ISSN 0285-6808

THE INSTITUTE OF SPACE AND ASTRONAUTICAL SCIENCE REPORT NO. 680

Actively Controlled Magnetic Bearing Momentum Wheel and Its Application to Satellite Attitude Control

By

Yong-Chun XIE, Hideyuki SAWADA,

Tatsuaki HASHIMOTO and Keiken NINOMIYA

March 2001

The Institute of Space and Astronautical Science, Kanagawa

ISAS REPORT No. 680 (March) 2001

Published by The Institute of Space and Astronautical Science(ISAS)
3-1-1 Yoshinodai, Sagamihara, Kanagawa, 229-8510, Japan
Fax : +81-42-759-8440
E-mail : newsedit@adm. isas. ac. jp

Printed FUJIWARA Printing CO., LTD.
3-6-4 Fujimidai, Kunitachi, Tokyo, 186-0003, Japan.

CONTENTS

The Institute of Space and Astronautical Science
Report No. 680, March 2001

Actively Controlled Magnetic Bearing Momentum Wheel and Its Application to Satellite Attitude Control

By

Yong-Chun XIE*, Hideyuki SAWADA**, Tatsuaki HASHIMOTO** and Keiken NINOMIYA**

(February 22, 2001)

ABSTRACT: For the high-accuracy attitude control of spacecraft, Magnetic Bearing Momentum Wheel (MBMW) has been being investigated as an actuator because of its merits of low disturbance characteristics and "gimballability" when a suitable active controller is used. The active control of MBMW in this context means to make the rotor spin around its principal axis of inertia to achieve low disturbance purpose while being able to tilt the principal axis of inertia for attitude control of spacecraft, and this has to be done with adequate nutation damping.

In previous literature with respect to the active control of MBMW, considering the non-linearity of electromagnets, Nam et al. [1] applied the H_∞ robust control method to the active control of MBMW, but only a fixed rotational speed is considered. Without thinking of the non-linearity of electromagnets, Bichler [2] proposed a Model Following Control (MFC) method and indicated that this method has superior capability of active-vibration suppression for a large range of wheel rotational speed. However, this method is based on a special observer to realize active-vibration suppression, thus its response to fast externally exerted torque and movements is slow. If externally exerted disturbance torque, including those due to eddy current loss, ohmic loss and those exerted from the spacecraft body on which the physical space-environmental torque acts exist, large overshoot and small nutation of the wheel rotor will be excited when wheel rotational speed is low. Therefore, to realize the active control of MBMW with non-linear electromagnets, an Adaptive Model Following Control (AMFC) method is proposed in this report.

In this new method, first an adaptive mechanism is inserted in the above model following control method. This adaptive mechanism can adaptively regulate the bandwidth of a special observer based on on-line identification of state characteristics so as to improve system dynamic response if needed and to make compromise between fast dynamic response and active-vibration suppression at harmonic frequencies of the wheel rotation. Second, logical derivative [3] is applied to the controller design to reduce overshoot further. Third, a new nutation damping method that can automatically adjust the gain of nutation damping according to wheel speed is introduced in order to obtain consistent damping rate for different wheel speed. Finally, a non-

* C.O.E. (Center of Excellence) research fellow of Institute of space and Astronautical Science on leave from Beijing Institute of Control Engineering, P. R. China.
** Institute of space and Astronautical Science, 3-1-1 Yoshinodai, Sagamihara, 229-8510, Japan.

linearity compensator is put forward to overcome electromagnetic non-linearity. The advantage of this method is that it is easy to make compromise between nutation damping and disturbance suppression at harmonic frequencies of the wheel rotation. Since the closed-loop system is non-linear and time-varying system, the stability and robustness of this method is analyzed from the engineering viewpoint.

A large amount of simulation has been done. The simulation results show that the AMFC method has great capability of disturbance suppression, good dynamic response and satisfactory nutation damping for a large range of wheel speed. Therefore it is possible to realize high accuracy attitude control by using the MBMW controlled by the AMFC method as actuator.

How to apply the MBMW controlled by the AMFC method to satellite attitude control is also studied in this report. As an example, Solar-A Satellite is selected to examine the effectiveness of this method.

The report is organized as follows. In Chapter 1, the active control of magnetic bearing including MBMW is reviewed. In Chapter 2, MBMW including structure and its mathematical model is introduced. In Chapter 3, the adaptive model following control method is presented and its performance, stability and robustness are analyzed in Chapter 4. To verify the effectiveness of this new method digital simulation is carried out in Chapter 5, in which, AMFC, MFC and H_∞ method are compared. In Chapter 6, the possible application of the AMFC method to the active control of MBMW for spacecraft attitude control is discussed. Finally, some conclusion is given in Chapter 7.

1 INTRODUCTION

Magnetic Bearing Momentum Wheels (MBMW) are suspended by magnetic bearings. For good understanding of the active control of MBMW, magnetic bearings and the active vibration control methods of magnetic bearings are reviewed first. Then actively controlled MBMW and its application to satellite attitude control are surveyed.

1.1 MAGNETIC BEARINGS

Active magnetic bearings (AMB) are bearings where the suspension forces for supporting the rotors are generated magnetically without any contact. Compared with ball bearings, active magnetic bearings have the advantages as no contact and lubrication, allowing high-speed rotation and providing active vibration control. Therefore, as an attractive technology, AMB could be applied to high-speed rotating machinery like turbo pumps [4], flywheels for energy storage [5], reaction wheels for attitude control of spacecraft [1, 2], the main shafts of electric motors of tool machines and turbo compressors [6, 7, 8].

Although magnetic bearings should be on first glance ideally suited to exhibit low noise figures because of no mechanical contact between stator and rotor, unfortunately there are still several possible sources of disturbing forces and torque in magnetic bearings.

The main source is imbalance, which means that the geometric axis of rotor is not coincident with the principal axis of inertia. In a magnetic bearing the rotational axis of rotor is the axis of the position sensor or gap sensor measurement surface. Thus if the rotor spins about its principal axis of inertia, the measurement surface wobbles. If the rotor is made to spin about its geometric

axis, an unbalance force will be produced.

The other sources include mechanical imperfections of the rotating part, sensor electric inevitable imperfection and sensor asymmetry in location. The mechanical imperfections of the rotating part, which can be regarded as irregularities in a sensor surface, could lead to harmonic noise in sensor signals. Sensor electric imperfection may bring sensor noise usually modeled as band-limited white noise. And sensor asymmetry in location might cause measurement coupling between different loops.

Besides the above sources, the non-linearity of electromagnets may cause disturbing forces or torque as well.

Furthermore, although their amplitude is small, externally exerted disturbance torque still exist. For MBMW, the externally exerted disturbance torque include those due to eddy current loss, ohmic loss and those exerted from the spacecraft body on which the physical space-environmental torque acts.

As a result, the active vibration control or unbalance control of magnetic bearings is the most important problem in applying magnetic bearings to a rotor system for improving the performance of industrial and space applications.

1.2 Active Vibration Control Methods

In the area of active elimination of unbalance vibration, voluminous studies have been done since the pioneer work of [9]. There are two ways to solve the above imbalance problem of magnetic bearings. The first is called compensation for unbalance. With this method, electromagnetic forces are generated to cancel the unbalance forces and the rotor precisely rotates around the geometrical axis [6, 8, 10, and 11]. The other is called automatic balancing control. By using this method, the spinning axis corresponds with the principal axis of inertia and no compensative force or torque is needed [4, 12]. In general, compensation for unbalance is adopted when precise direction of rotor is required while automatic balancing control is taken if housing vibration is unacceptable.

To overcome the non-linearity of electromagnets, a linear AMB model is obtained by using a constant pre-magnetization bias current I_0 in each coil of the AMB, and carrying out a linearization at (I_0 ,e_0), where e_0 is the nominal air gap. In this case, several methods for reducing the effect of the unbalance on the displacements or on the forces created by the coils have been presented.

- Adaptive open-loop feed-forward compensation methods add a synchronous signal to the control signal. The amplitude and phase of the synchronous signal are adaptively adjusted so as to cancel or minimize the synchronous housing vibration. The way to generate this synchronous signal and the adaptation process to adapt the compensation signal to the unknown rotor unbalance may be different [13, 14, 15, and 16]. Since these methods operate external to the stabilizing control loop, they do not affect loop stability. The main problem of these methods is the proof of convergence.

- Notch filters insert notch filters into the control loop so that synchronous signal components in the feedback loop are cancelled and hence no synchronous forces can be generated by magnetic bearing [2, 4, 14]. The major drawback of the early notch approaches is that the

closed-loop stability may be lost due to the insertion of an open-loop designed filter into a closed-loop setup [4]. Herzog et al. [4] tried to solve this problem by a posterior insertion of a generalized notch filter under the assumption that the rotational speed is measurable .

- Observer based methods construct a controller based on the state-space approach, for example output regulator, to preserve internal stability and reject the disturbance [12, 17]. These methods require an accurate plant model, including unbalance disturbance model, which is the function of the rotational speed. These methods can deal with both ”compensation for unbalance” and ”automatic balancing control”, whether the error to be fed back is disturbance force/torque or sensor output.

- H_∞ robust controller and μ synthesis controller, as well known, are robust with respect to unmodeled dynamics, parameter uncertainty and disturbances. By treating the vibrations caused by unbalance of a rigid rotor as frequency-varying sinusoidal disturbance, gain scheduled H_∞ robust controller was presented in [6]. This method can eliminate frequency-varying sinusoidal disturbance and makes the rotor spin about its geometric axis precisely. Nam et al. [1] manifested the robustness of H_∞ controller against electromagnetic non-linearity, which is modeled as disturbance torque. This controller can also eliminate disturbance torque caused by rotor unbalance and the method is considered as one of the ”automatic balancing control”. In these methods, it is common that disturbance rejection and sensor error suppression are obtained by choosing two weighting functions as loop shaping functions. For general understanding, it should be mentioned that H_∞ robust controller and μ synthesis controller are intensively studied in the area of flexible rotor magnetic bearings [7, 10]. The reason is that H_∞ robust controller and μ synthesis controller are strongly robust to unmodeled higher order dynamics of flexible rotor and parameter errors in rotor and electromagnets. The main problem concerned with these methods is the resulting controller order is usually quite large for implementation on a single digital signal processor with high sampling rates.

- Sliding mode control is also robust to modeling error and disturbances. Therefore, sliding mode control can carry out compensation for unbalance by representing rotor imbalance as sinusoidal disturbance force/torque [8, 18]. In sliding mode controller design, disturbance rejection is submerged in equilibrium manifold design and an observer is rendered to state and disturbance estimation. The robustness of this method with respect to rotor speed in a certain range was examined in [8]. The convergence of the observer may affect the performance of system response.

- Other methods include model following control [2], adaptive auto-centering control [19], Fuzzy Logic [20], and etc.

  The principle idea of the model following control is to use the output of an observer, simply a double integrator, for the feedback control. The observer output is well suited for low noise purposes, because it almost does not contain any disturbances. Model following control was considered as the superior automatic balancing control method in [2], because it offers very good noise suppression, which increases with frequency, and the closed-loop stability is guaranteed. However, its robustness to external disturbances and parameter uncertainty still needs to be examined together with the controller included.

  Based on the notion that physical imbalance is independent of the spin rate, an adaptive auto-centering control was presented in [19]. This method involves on-line estimation of the

center of mass position and velocity and incorporation of these into a feedback control. This has the advantage that the estimation can be discontinued after convergence and the values so determined can be used over a range of operating speed. Under the proposed control law, the rotor achieves rotation about the mass center and principal axis of inertia. To apply this method to high-speed industrial applications where rotors exhibit flexible behavior is still under consideration.

In [20] a fuzzy derivate gain adjusting method was presented based on the error and error derivate signals that are used as the basis of the fuzzy inference. The main idea of this method is to adjust the derivate gain of a traditional controller, a PID controller in [20], in order to decrease the effect of sensor noise on system responses.

In [2,21, 22] some of the above methods were compared by simulation and/or experiment.

In the design of active vibration control strategy for high-speed spinning rotors, two problems usually have to be considered carefully to avoid instability and to achieve good system performance. The first is gyroscopic effect when rotors have a no small ratio of the moments of inertia, e. g., pumps, turbines, and especially flywheels [5, 23]. The other is sampling period if digital control is used [24].

1.3 Actively Controlled MBMW and its Application to Spacecraft Attitude Control

It is well known that momentum wheels and reaction wheels are main actuators of spacecraft attitude control systems. However, conventional momentum wheels and reaction wheels with ball bearings are significant sources of force and torque noise, which may degrade spacecraft attitude-pointing stability. The stiff ball bearings transmit flywheel unbalance forces into the spacecraft structure and lubricants contribute drag torque, torque disturbance and stiction. To avoid this problem and to meet the stringent requirements of spacecraft attitude pointing accuracy that is becoming higher and higher, low noise magnetically suspended momentum wheels or MBMW have been considered as promising alternatives for spacecraft attitude control [2,25,26,27].

The merits of MBMW come from no contact and no lubrication between stator and rotor, allowing high-speed rotation and providing gimballing capability. Therefore, compared with ball-bearing type wheels, MBMW have the advantages as low disturbance, long life and gimballability. The low disturbance is very important feature for high accuracy earth-observation and/or scientific missions of the near future. For example, Solar-B mission of ISAS, a solar observatory satellite to be launched in 2004, requires sub-arcsec order pointing stability. The last feature means that in principle only one wheel is enough to control three axes of spacecraft, thus saving actuator weight as compared with the 3-minimum sets of ball bearing type wheels required generally to control the three axes of spacecraft.

As other magnetic bearings, the active control of MBMW is the most important problem in applying MBMW to high quality attitude control of spacecraft. For MBMW, theoretically, if a suitable active control law is applied to make the rotor spin at a constant speed exactly about its principal axis of inertia, there will be no disturbance torque from the MBMW working on the spacecraft. Therefore, in this context, the active control of MBMW means to make the rotor spin around its principal axis of inertia to achieve low disturbance purpose while being able to tilt the principal axis of inertia for attitude control of spacecraft. And this has to be done with adequate

nutation damping of the wheel rotor.

According to the above discussion, in order to realize high-accuracy attitude control of spacecraft, the active control system of MBMW must satisfy the following performance requirements.

(1) Good active-vibration suppression under existence of inevitable error on sensor system. Since the band-limited white noise is easy to be suppressed by using a low pass filter, the components to be suppressed by means of active-vibration suppression are mainly those disturbance components with harmonic frequencies of the wheel rotation. In fact, the disturbance incurred as a result of the nutation damping is inevitable, but it can be suppressed below an acceptable level by the design of the control system. In [2] Active-Vibration Suppression (AVS) is defined, which means to enable the rotor rotating about its principle axis of inertia and suppress all the resulting noise components from the whirling and wobbling sensor surface without affecting the suspension stability. This term is adopted through this report.
(2) Robustness against electromagnetic non-linearity.
(3) Good disturbance suppression by MBMW against wheel's externally exerted disturbance torque. This and the following item (4) are partly the theme to be dealt with in the attitude control system design as well.
(4) Robustness against wheel rotational speed in a large range.

In previous literature, considering the non-linearity of electromagnets, Nam et al. [1] applied the H_∞ robust control method to the active control of MBMW, but only a fixed rotational speed is considered. Without thinking of the non-linearity of electromagnets, Bichler [2] proposed a Model Following Control (MFC) method and indicated that this method has superior capability of active-vibration suppression for a large range of wheel rotational speed. However, this method is based on a special observer to realize active-vibration suppression. Thus its response to fast externally exerted torque and movements is slow. If externally exerted disturbance torque, e. g. reaction torque due to fast movement of optical filters in onboard scientific instruments/optics-systems and the disturbance torque which has been mentioned already exist, large overshoot and small nutation of the wheel rotor will be excited when wheel rotational speed is low. Therefore, in order to solve the above problems and to realize the active control of MBMW with non-linear electromagnets, an Adaptive Model Following Control (AMFC) method is proposed in this report.

In this new method, first an adaptive mechanism is inserted into the above model following control method. This adaptive mechanism can adaptively regulate the bandwidth of a special observer based on on-line characteristic identification so as to improve system dynamic response if needed. Second, logical derivative [3] is applied to the controller design to reduce overshoot further. Third, a new nutation damping method that can automatically adjust the gain of nutation damping according to wheel speed is introduced in order to obtain consistent nutation damping rate for different wheel speed. Finally, a non-linearity compensator is put forward to overcome electromagnetic non-linearity. Consequently, the adaptive model following control method is competent for the active control of MBMW.

2 MBMW

Although the control method presented in this report could be applied to any actively controlled MBMW, the authors pick up a specific type of MBMW and apply the method to the control of this kind of wheel.

2.1 OCTA-ELECTROMAGNET-TYPE ACTIVE MAGNETIC BEARING MOMENTUM WHEEL

For future three-axis spacecraft attitude control, Octa-Electromagnet-Type Active Magnetic Bearing Momentum Wheel (OETA-MBMW), which is a kind of five-degree of freedom MBMW, is developed in ISAS [1, 28]. OETA-MBMW is composed of eight electromagnets whose attractive forces have components both in axial and in radial direction so that it may serve to reduce size and weight. Eight gap sensors are symmetrically installed with tilts so as to measure the rotor displacements in three directions and gimbaling angles around two axes vertical to the wheel rotational axis. The cross section of this kind of OETA-MBMW is shown in Fig. 2.1.

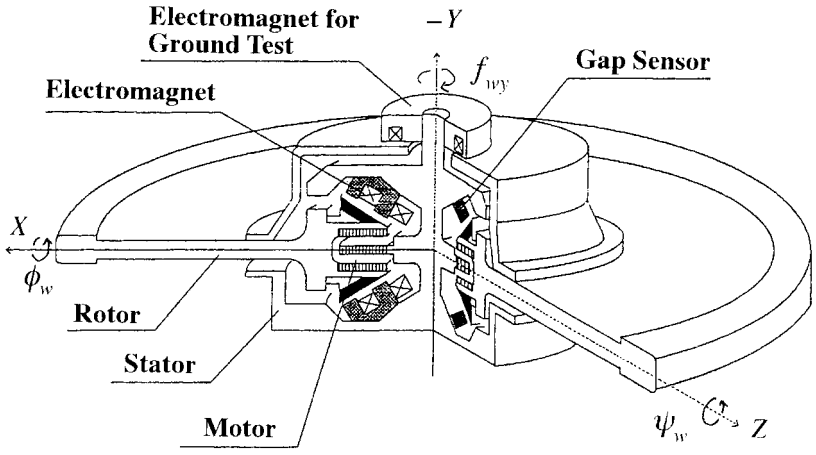

Fig.2.1 Cross section of Octa-Electromagnet-Type Active Magnetic Bearing Momentum Wheel

2.2 WHEEL DYNAMICS

In describing the rotational motion of the MBMW, rotational coordinate systems are used as shown in Fig. 2.2, in which coordinate system $X_0Y_0Z_0$ is defined here as spacecraft's attitude reference coordinate system, while $X_wY_wZ_w$ a wheel-rotor-fixed coordinate. $X_0Y_0Z_0$ changes so slowly in inertial space that it can be considered as an inertial coordinate system for the present purpose. Angles ϕ_w, φ_w and θ_w are the Euler angles in X-Z-Y transformation from $X_0Y_0Z_0$ to $X_wY_wZ_w$. For the simplicity of motion derivation, spin-free coordinate system $X_{2w}Y_{2w}Z_{2w}$ is used to describe the dynamic motion of MBMW [1].

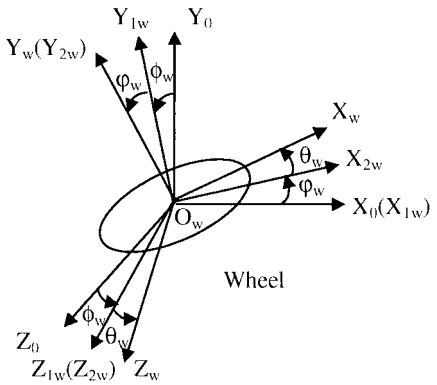

Fig. 2.2 Coordinate systems of MBMW

The Euler equation of wheel dynamic motion in $X_{2w}Y_{2w}Z_{2w}$ can be expressed as follows.

$$\dot{\boldsymbol{H}}_w + \Omega_{2w} \times \boldsymbol{H}_w = \boldsymbol{T}_w . \tag{2.1}$$

$$\boldsymbol{H}_w = \boldsymbol{J}_w \omega_w . \tag{2.2}$$

Where

$$\begin{cases} \boldsymbol{H}_w : \text{ angular momentum of wheel,} \\ \boldsymbol{J}_w : \text{ inertial tensor of wheel,} \\ \omega_w : \text{ angular rate of wheel,} \\ \Omega_{2w} : \text{ angular rate of } X_{2w}\, Y_{2w}\, Z_{2w}, \\ \boldsymbol{T}_w : \text{ outer Torque.} \end{cases}$$

Suppose that the following assumptions are satisfied,

(A 1) the selected coordinate is on principal axes,
(A 2) the wheel is rigid and symmetric about its rotational (pitch) axis.

Then we have,

$$\begin{cases} \boldsymbol{J}_w = J_w \boldsymbol{i}_{2w} + J_{wy} \boldsymbol{j}_{2w} + J_w \boldsymbol{k}_{2w} , \\ \omega_w = \dot{\phi}_w \cos\varphi_w \boldsymbol{i}_{2w} + (\dot{\theta} - \dot{\phi}_w \sin\varphi_w) \boldsymbol{j}_{2w} + \dot{\varphi}_w \boldsymbol{k}_{2w} \\ \Omega_{2w} = \dot{\phi}_w \cos\varphi_w \boldsymbol{i}_{2w} - \dot{\phi}_w \sin\varphi_w \boldsymbol{j}_{2w} + \dot{\varphi}_w \boldsymbol{k}_{2w} \\ \boldsymbol{H}_w = H_{wx} \boldsymbol{i}_{2w} + H_{wy} \boldsymbol{j}_{2w} + H_{wz} \boldsymbol{k}_{2w} , \\ \boldsymbol{T}_w = T_{wx} \boldsymbol{i}_{2w} + T_{wy} \boldsymbol{j}_{2w} + T_{wz} \boldsymbol{k}_{2w} . \end{cases} \tag{2.3}$$

Where J_{wx}, J_{wy} and $J_{wz}(J_{wx} = J_{wz} = J_w)$ are principal moments of inertia along X_w, Y_w and Z_w respectively, and H_{wx}, H_{wy}, H_{wz} are respectively the angular momentum vector components of the wheel-rotor along X_w, Y_w, Z_w axis.

By substituting (2.3) into (2.1) and (2.2), (2.1) and (2.2) can be rewritten as follows.

$$\begin{cases} \dot{H}_{wx} = H_{wz}\dot{\phi}_w \sin\varphi_w + H_{wy}\dot{\varphi}_w + T_{wx} \\ \dot{H}_{wy} = -H_{wx}\dot{\varphi}_w + H_{wz}\dot{\phi}_w \cos\varphi_w + T_{wy} \\ \dot{H}_{wz} = -H_{wy}\dot{\phi}_w \cos\varphi_w - H_{wx}\dot{\phi}_w \sin\dot{\varphi}_w + T_{wz} \end{cases}. \tag{2.4}$$

$$\begin{cases} \dot{\phi}_w = H_{wx}/(J_w \cos\varphi_w) \\ \dot{\theta}_w = H_{wy}/J_{wy} + \dot{\phi}_w \sin\varphi_w \\ \dot{\varphi}_w = H_{wz}/J_w \end{cases}. \tag{2.5}$$

Define state variables as follows,

$$\begin{cases} x_0 = H_{wx}/J_w \\ x_1 = H_{wy}/J_{wy} \\ x_2 = H_{wz}/J_w \\ x_3 = \phi_w \\ x_4 = \theta_w \\ x_5 = \varphi_w \end{cases}. \tag{2.6}$$

Then, according to (2.4) and (2.5), we obtain the following state equations for wheel dynamic motion.

$$\begin{cases} \dot{x}_0 = \left[T_{wx} + (J_w x_0 \tan x_5 + J_{wy} x_1) x_2\right]/J_w \\ \dot{x}_1 = T_{wy}/J_{wy}, \\ \dot{x}_2 = \left[T_{wz} - (J_w x_0 \tan x_5 + J_{wy} x_1) x_0\right]/J_w \\ \dot{x}_3 = x_0/\cos x_5 \\ \dot{x}_4 = x_1 + x_0 \tan x_5 \\ \dot{x}_5 = x_2 \end{cases}. \tag{2.7}$$

For control system design, a simplified model is used. Suppose that the selected coordinates are on the principal axes as already assumed, the gimbaling angles of MBMW are small, the wheel is rigid and symmetric about its rotational axis, and the wheel rotational speed $\dot{\theta}_w$ varies so slowly with time that it can be considered as constant [1]. Then the linearized dynamic model of MBMW in gimbaling axes can be expressed as follows.

$$\begin{cases} \ddot{\phi}_w - \sigma\Omega\dot{\varphi}_w = (T'_{wx} + T_{dx})/J_w \\ \ddot{\varphi}_w + \sigma\Omega\dot{\phi}_w = (T'_{wz} + T_{dz})/J_w \end{cases}. \tag{2.8}$$

In (2.8), $\sigma = J_{yw}/J_w$ is the ratio of moments of inertia. $\Omega = \dot{\theta}_w$ is wheel rotational speed. T'_{wx} and T'_{wz} are electromagnetic torque. T_{dx} and T_{dz} are externally impressed disturbance torque including those due to eddy current loss, ohmic loss, fast movement of optical filters in onboard scientific instruments/optics-systems and those exerted from the spacecraft body on which the physical space-environmental torque acts. $T_{wx} = T'_{wx} + T_{dx}$ and $T_{wz} = T'_{wz} + T_{dz}$.

2.3 ELECTROMAGNETS

According to experimental data, the torque by electromagnet can be modeled accurately enough as follows [28].

$$\begin{cases} T'_{wx} = k_m \phi_g^2 \left(\dfrac{V_b + v_\phi}{\phi_g - \phi} \right)^2 - k_m \phi_g^2 \left(\dfrac{V_b - v_\phi}{\phi_g + \phi} \right)^2 \\ T'_{wz} = k_m \varphi_g^2 \left(\dfrac{V_b + v_\varphi}{\varphi_g - \varphi} \right)^2 - k_m \varphi_g^2 \left(\dfrac{V_b - v_\varphi}{\varphi_g + \varphi} \right)^2 \end{cases}. \tag{2.9}$$

In (2.9), k_m is electromagnetic gain, ϕ_g and φ_g are constants calculated from the nominal electromagnetic gaps, ϕ and φ are electromagnetic gaps or tilt angles, and satisfy $|\phi| < \phi_g$, $|\varphi| < \varphi_g$. If we neglect the attitude motion of spacecraft, then $\phi = \phi_w$ and $\varphi = \varphi_w$. V_b is a constant representing bias voltage applied to electromagnets, v_ϕ and v_φ are control commands or control voltages, and satisfy $|v_\phi| < V_b$, $|v_\varphi| < V_b$.

As an example, the electromagnetic non-linearity characteristics of a prototype MBMW owned by Professor Ninomiya's laboratory are shown in Fig. 2.3 with tilt (or gimbal) angle as the parameter and for the bias voltage $V_b = 0.8$V. According to Fig. 2.3, we know that the electromagnetic non-linearity is still serious for control system design, although bias voltage is used to weaken the strong non-linearity of electromagnets.

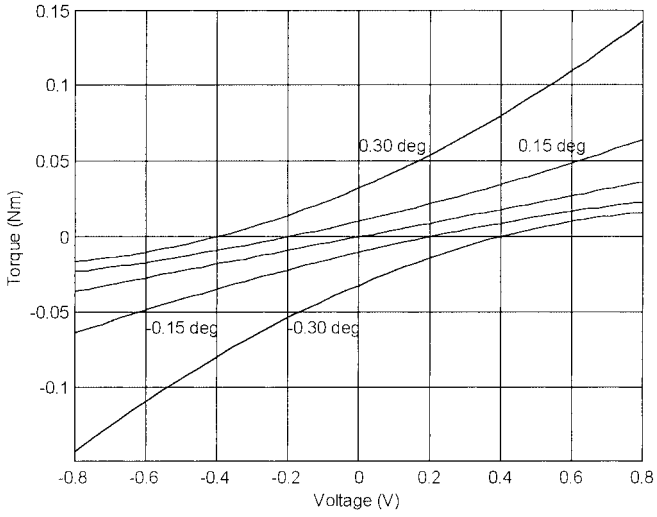

Fig. 2.3 Characteristics of electromagnetic non-linearity

According to (2.9) we know that the non-linearity of electromagnets is proportional and inversely proportional in the second order for voltage-input and the gimbaling angles of the wheel, respectively. Although, in order to overcome this kind of electromagnetic non-linearity, a constant pre-magnetization bias voltage V_b is added, the electromagnetic torque-output is still not pure linear

function of control voltage-input. By using Taylor expansion, the first-order approximation of (2.9) can be expressed in (2.10).

$$\begin{cases} T'_{wx} = k_{EM} v_\phi + k_{N\phi} \phi \\ T'_{wz} = k_{EM} v_\varphi + k_{N\varphi} \varphi \end{cases}. \tag{2.10}$$

Where $k_{EM} = 4k_m V_b$, $k_{N\phi} = 4k_m V_b^2 / \phi_g$, $k_{N\varphi} = 4k_m V_b^2 / \varphi_g$.

2.4 GAP SENSORS

Following sensor noises (or rather output signals) of MBMW are considered in gap sensor model according to wheel mechanism [28].

(1) Sensor noise resulting from the electric noise components of gap sensors is modeled as white noise ($\zeta_\phi, \zeta_\varphi$)whose frequency band is limited roughly to the controller's sampling frequency.

(2) Harmonic sensor noises caused by imbalance of rotor (i.e. the geometric axis of rotor is not coincident with the principal axis of inertia) and mechanical imperfections of the rotating part surface are modeled with the harmonic signals of wheel rotational speed shown as follows.

$$\begin{cases} n_\phi = \sum_{i=1}^{N_s} c_i \sin(i * \theta_w + \theta_i) \\ n_\varphi = \sum_{i=1}^{N_s} c_i \sin(i * \theta_w + \theta_i + \pi/2) \end{cases}. \tag{2.11}$$

In (2.11), N_s is the number of harmonics, c_i is the amplitude of harmonics, and θ_i is initial angle.

As a result, the model of gap sensors can be expressed in (2.12).

$$\begin{cases} \tilde{\phi}_w = \phi_w + \sum_{i=1}^{N_s} c_i \sin(i * \theta_w + \theta_i) + \zeta_\phi \\ \tilde{\varphi}_w = \varphi_w + \sum_{i=1}^{N_s} c_i \sin(i * \theta_w + \theta_i + \pi/2) + \zeta_\varphi \end{cases}. \tag{2.12}$$

Denote the sum of all sensor noises as

$$\begin{cases} \xi_\phi = n_\phi + \zeta_\phi \\ \xi_\varphi = n_\varphi + \zeta_\varphi \end{cases}. \tag{2.13}$$

Then (2.12) can be rewritten as

$$\begin{cases} \tilde{\phi}_w = \phi_w + \xi_\phi \\ \tilde{\varphi}_w = \varphi_w + \xi_\varphi \end{cases}. \tag{2.14}$$

In the next Chapter the active control of the MBMW shown in (2.7), (2.9) and (2.12) will be studied according to its simplified model (2.8), (2.10) and (2.12).

3 ADAPTIVE MODEL FOLLOWING CONTROL METHOD

AMFC method is proposed based on MFC method [2], thus it keeps the basic structure of MFC method and inherits MFC's advantages. However, AMFC method is superior to MFC method because of its adaptive mechanism for active vibration suppression, controller with logical derivative, new nutation damping strategy and non-linearity compensator.

The block diagram of the AMFC closed-loop system for the active control of the rotor-tilt-loops of MBMW is shown in Fig. 3.1. In fig. 3.1, the right part enclosed by dash-line frame represents the plant to be controlled, i.e. MBMW, while the other left part represents AMFC's control loop. According to Fig. 3.1 we know that AMFC is composed of Adaptive Model Following Active-Vibration Suppression (AMF-AVS), tilt angle controller, gyro-decoupling network, nutation damping network and non-linearity compensator. Since all of these five parts have explicit physical meanings, they are easy to be designed and to be applied to different MBMWs. In the following sections the meaning and function of each part of Fig. 3.1 will be explained in detail.

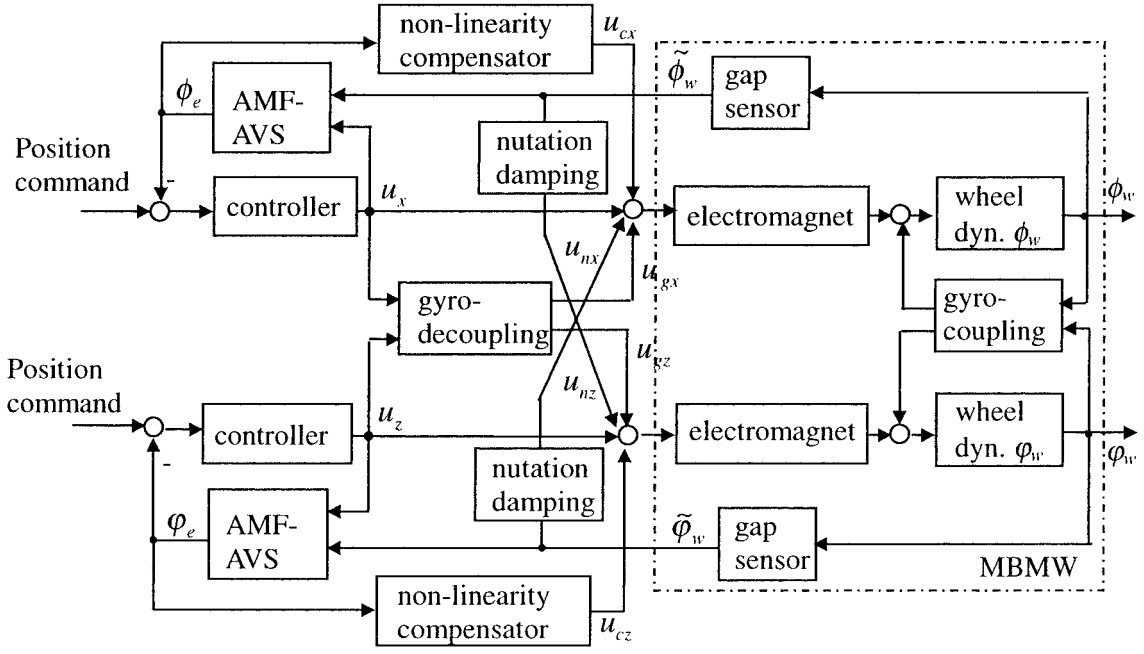

Fig. 3.1 AMFC in the tilt loops of MBMW

3.1 MBMW

Wheel dynamics refers to (2.7).
Gap sensor refers to (2.9).
Electromagnet refers to (2.12).

3.2 GYRO-DECOUPLING NETWORK

When the wheel is rotating, gyro-couplings between the tilt axes of the wheel arise, which are proportional to the speed and which enable the precessional and nutational oscillations. The highest nutational frequency of a flat rotor is about twice the speed. A tilt controller, which copes with the frequency, must be of wide bandwidth and therefore causes an increased power demand in the actuator due to noise. Further more the AMF-AVS that will be proposed in the following is not directly applicable to the gyro-coupled tilt loops, because then the model would not represent the real plant. One possibility to overcome these problems may be the introduction of a gyro-decoupling network, which distributes the controller outputs over both torque inputs and additionally improves the dynamic behavior of the tilt loops. Then each controller sees the same plant as if the wheel stands still and the observer remains the same as before.

In Fig. 3.1, gyro-decoupling network uses the same decoupling network proposed in [2], which is depicted in (3.1).

$$\begin{cases} u_{gx} = -\sigma_0 \Omega_0 \dfrac{1}{s} u_z \\ u_{gz} = -\sigma_0 \Omega_0 \dfrac{1}{s} u_x \end{cases} . \tag{3.1}$$

where, u_x and u_z are the inputs of the gyro-decoupling network while u_{gx} and u_{gz} the outputs. σ_0 and Ω_0 represent the nominal values of σ and Ω, respectively.

It should be mentioned that in this report, the variable with subscript 0 denotes the nominal value of this variable.

3.3 AMF-AVS

The block of AMF-AVS in Fig. 3.1 is demonstrated in Fig. 3.2. In Figure 3.2, AMFC-AVS is composed of integrator 1, integrator 2, low pass filter, adaptive mechanism, and some important coefficients, such as *gain*, k_{11}, k_{12}, k_{21} and k_{22}.

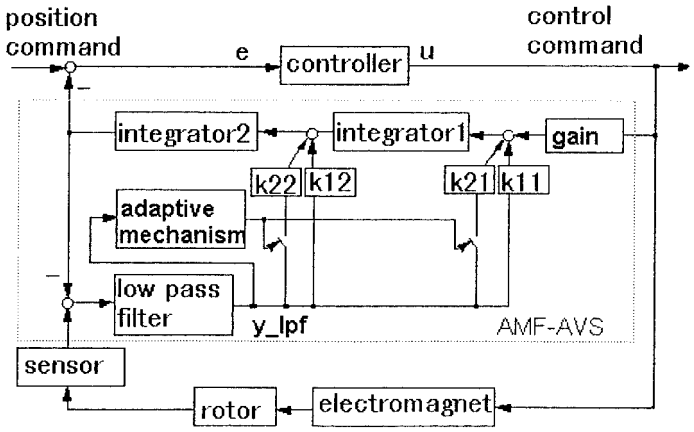

Fig. 3.2 Block diagram of AMF-AVS of AMFC

3.3.1 Integrator 1 and Integrator 2

Both integrator 1 and integrator 2 are standard integrators, whose transfer functions are $\frac{1}{s}$.

3.3.2 Low Pass Filter

To prevent the observer from long term drift effects, the low pass filtered difference between the real position signal and the model output is used to correct the observer's state variables. Therefore, the bandwidth of the low pass filter must cover the control bandwidth and leave the disturbance frequency out of it.

Low pass filter can be designed as a first-order low pass filter that can be represented as $\frac{a}{s+a}$, where a is positive real number.

3.3.3 *gain*

"*gain*" represents the gain coefficient of the plant to be controlled from electromagnet input to rotor output. For the plant discussed in this report, "*gain*" equals to k_{EM0}/J_{w0}, as defined above, where k_{EM0} and J_{w0} represent the nominal values of k_{EM} and J_w, respectively.

3.3.4 k_{11}, k_{12}, k_{21} and k_{22}

In Fig. 3.2, the AMF-AVS loop can be considered as a special adaptive observer of rotor movements. As gain vectors of the observer, $[k_{11}\ k_{12}]$ and $[k_{21}\ k_{22}]$ affect the convergence and bandwidth of the observer. Adaptive mechanism automatically determines when k_{21} and k_{22} should be switched on or switched off so that the bandwidth of AMF-AVS observer is regulated adaptively. Later we will discuss how to select these two gain vectors.

3.3.5 Adaptive Mechanism of AMF-AVS

In [2], to control the faster externally exerted stator movements, a limit switch is used to quicken the convergence of AVS observer by detecting the difference of the rotor real position and the observer output. If the difference exceeds half of the nominal gap, a second stronger feedback is turned on to force the observer output immediately to the real position to prevent a touch down of the rotor. The block diagram of AVS of MFC method is shown in Fig. 3.3. In fact, this kind of limit switch can not accommodate the faster externally exerted stator movements. The reason is that the limit switch works only after the difference exceeds half of the nominal gap, and even in this case stronger feedback in observer tends to result in larger controller output than the input voltage limit of the electromagnets, which means this effort is in vain. Furthermore, even the second stronger feedback works, the low noise quality of AVS is reduced because unfiltered sensor signal is introduced directly into the control system. In order to solve this problem and to make a good compromise between fast convergence of observer and satisfactory active-vibration suppression in the whole gap range, adaptive bandwidth-regulation method is proposed to replace the limit switch of MFC for AVS.

The main idea of the adaptive bandwidth-regulation method is to broaden the observer bandwidth when fast convergence is needed, for example when large overshoot occurs in gimbaling angles, and to reduce the observer bandwidth when active-vibration suppression is the main purpose, for example at the steady state. In this report steady state means the gimbaling angles are smaller

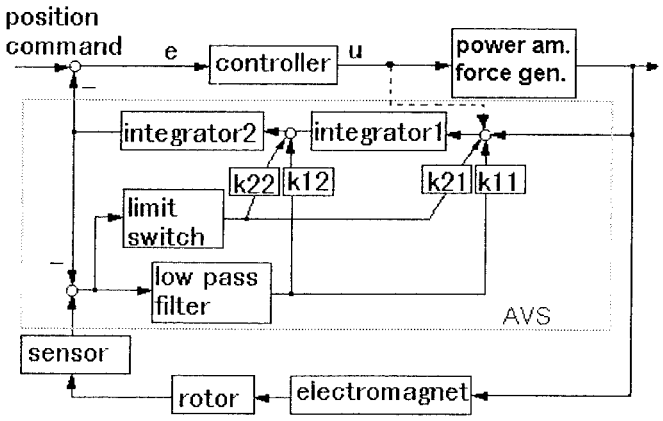

Fig. 3.3 Block diagram of AVS of MFC

than the required steady state errors continuously for a certain period of time. Moreover, In this method the saturation non-linearity of the input voltage of electromagnets is also considered. The adaptive bandwidth-regulation is based on on-line characteristic identification. The mechanism of the adaptive bandwidth-regulation is shown in Fig. 3.4.

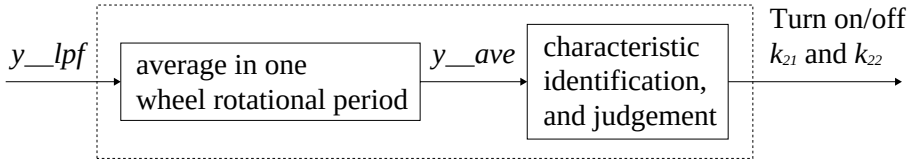

Fig. 3.4 Adaptive bandwidth-regulation mechanism for AVS

As defined in Fig. 3.2, y_lpf is the output of AMF-AVS low-pass filter. Define the average value of y_lpf in one wheel rotational period as y_ave. y_ave is refreshed every one wheel rotational period. The rule for determining when k_{21} and k_{22} should be turned on/off is depicted as follows.

Rule 3.1.

If $|y\_ave| > \delta_1$ and $|y\_ave| < \delta_2$,

then k_{21} and k_{22} are switched on,

else k_{21} and k_{22} are switched off.

In Rule 3.1, δ_1 is named as steady-state threshold, and is determined according to the index of steady state and the amplitude of sensor noises. δ_2 is named as saturation threshold, and is determined according to the input voltage limit of electromagnets and controller.

Rule 3.1 means that if the average difference of the observer output and the rotor position is much larger than the sensor noises and smaller than the saturation threshold, which can make sure the controller output is less than the input voltage limit, the bandwidth of AMF-AVS observer is broadened. This kind of bandwidth regulation can make the observer output follow the rotor posi-

tion quickly and effectively. Therefore the adaptive bandwidth-regulation method can improve system dynamic response while active-vibration suppression is guaranteed. The authors are aware, however, that the analysis does not constitute a rigorous proof of the robust stability of the system.

3.4 CONTROLLER WITH LOGICAL DERIVATIVE

The Controller can be designed as any kind of available style, if it can guarantee the closed-loop system consisting of this controller and the plant to be controlled stable and also can make the system response satisfactory. For the sake of simplicity, a Proportional-Integral-Derivative (PID) controller is designed first for tilting or gimbaling control.

For the titling loops, if the gyro-decoupling network and non-linearity compensator work well, then the plant to be controlled could be represented approximately by $\frac{k_{EM}}{J_w s^2}$. In Fig. 3.1, Controller can be designed as single-input and single-output controller because of the effect of gyro-decoupling network.

The controllers for ϕ_w axis and φ_w axis are the same and are depicted as

$$u = k_p e + k_i \int e dt + k_d \dot{e}. \tag{3.2}$$

In (3.2), u is controller output, e is the difference between position command and AMF-AVS observer output, k_p, k_i and k_d are proportional, integral, and derivative coefficients.

The closed-loop system consisting of plant $\frac{k_{EM}}{J_w s^2}$ and controller (3.2) has a characteristic polynomial, which is

$$J_w/k_{EM} s^3 + k_d s^2 + k_p s + k_i = 0. \tag{3.3}$$

Suppose the characteristic polynomial (3.3) can be expressed as

$$J_w/k_{EM}(s^2 + 2\zeta\omega + \omega^2)(s + b) = 0,$$

and let response frequency $\omega = 10$ rad/s, damping coefficient $\zeta = 0.707$, and $b = 1.5$, then $k_p = 121.21 J_w/k_{EM}$, $k_i = 150 J_w/k_{EM}$, $k_d = 15.64 J_w/k_{EM}$.

Logical derivative was proposed in [3] to improve system dynamic response, especially to reduce system overshoot. Therefore the above designed PID controller is modified to a controller with logical derivative. In fact, this kind of modification is very simple because only the derivative coefficient of the PID controlled is modified according to a certain logical rule.

After introducing logical derivative the controller for single-axis gimbaling control is designed as follows.

$$u = k_p e + k_i \int e dt + k'_d \dot{e}. \tag{3.4}$$

Where

$$\begin{cases} k'_d = k_d & if\ (e\dot{e} \le 0\ or\ in\ steady\ state) \\ k'_d = k_{logic}\ k_d & else \end{cases}$$

k'_d is logical derivative coefficient, k_{logic} is the modifying coefficient for logical derivative and $k_{logic} \geq 1$. As discussed above, if $|e| < \delta_3$ is satisfied continuously for more than N_s sampling periods then we say that system is' *in steady state'*. Where δ_3 is the required steady state error and N_s is positive integer.

In the transient process, suitable k_{logic} leads to high controller bandwidth and phase lead, thus logical derivative can improve system dynamic response. However, in the steady state, the controller with logical derivative becomes a standard PID controller. Hence logical derivative doesn't affect the stability of the whole control system [3].

3.5 NUTATION DAMPING

As we know that for a high-speed rotating wheel, if there is impulsive torque vertical to the rotational axis working on the wheel, nutation of the rotating wheel will be excited. For a given torque, the lower the wheel rotational speed is, the larger the nutation amplitude is. The nutation frequency of the wheel equals to $\sigma\Omega$. For a flat wheel $\sigma > 1$, accordingly the nutation frequency of the rotating wheel usually is so high that it is beyond the tilt or gimbaling controller's bandwidth. Therefore, active nutation damping of the rotating rotor is necessary for the active control of MBMW. In practice, the coil of electromagnets tends to result in time delay. This kind of time delay together with other time delay caused by control loop make the active nutation damping of MBMW very difficult.

To solve the above problem, a new nutation damping strategy is proposed to damp down the nutation deteriorated by AMF-AVS and wheel's externally exerted disturbance torque. The nuta-

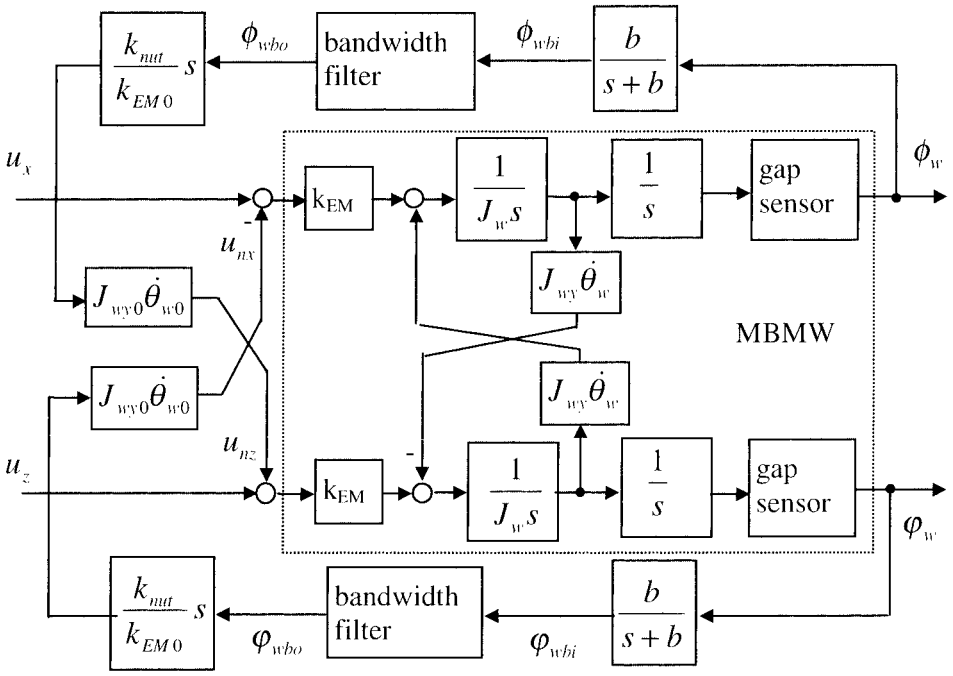

Fig. 3.5 Block diagram of nutation damping

tiondamping cross coupling network for tilt loops is shown in Fig. 3.5.

In Fig. 3.5 a bandwidth filter, whose transfer function is $\frac{\varkappa s}{s^2+\varkappa s+(\sigma_0\Omega_0)^2}$, is introduced to extract nutation component, where $\varkappa$ is a positive real number. It should be mentioned that smaller $\varkappa$ results in narrower filter bandwidth and accordingly better disturbance suppression in nutation damping loop. However, too small $\varkappa$ may cause realization problem in digital control system. Therefore a technical realization of the bandwidth filter is proposed in this report, which is shown is Fig. 3.6.

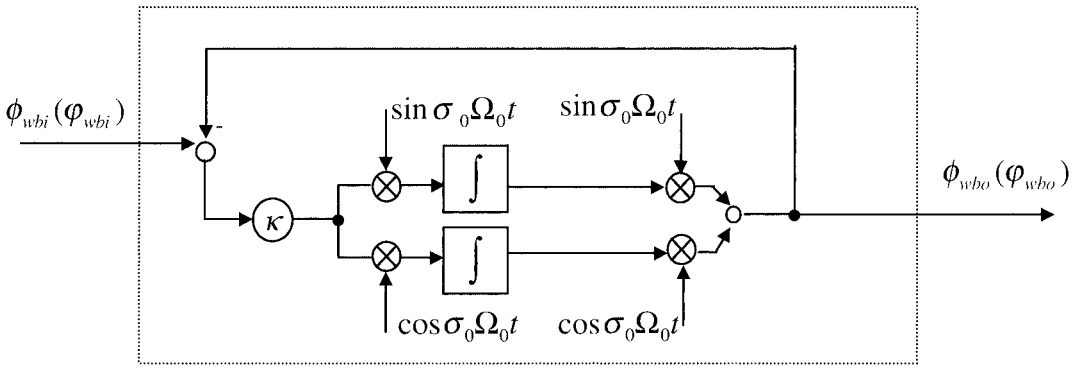

Fig. 3.6 Block diagram of a realization of the bandwidth filter in Fig. 3.5

Besides the bandwidth filter, in Fig. 3.5, $\frac{b}{s+b}$ is a low pass filter, where b is positive real number. The low pass filter aims to keep band-limited white noise and high-frequency disturbance components out of nutation damping loop. Here, the high-frequency disturbance components include those disturbance components with harmonic frequencies of the wheel rotation, and those disturbance components with mixed frequencies of harmonic frequencies of the wheel rotation and nutation frequency, which are caused by electromagnetic non-linearity. Moreover, in Fig. 3.5, k_{nut} is nutation damping gain and $k_{nut} > 0$.

The advantage of this nutation damping method is that the declining rate of nutation damping is independent of wheel rotational speed because the parameters of the nutation-damping network are functions of wheel rotational speed. In addition, by choosing a suitable nutation-damping gain, this nutation damping method is easy to realize nutation damping for MBMW with large time-delay of the driving circuits of the electromagnets.

3.6 NON-LINEARITY COMPENSATOR

Since electromagnetic non-linearity will cause disturbance torque, a compensator for this kind of non-linearity is necessary in the active control of MBMW.

According to (2.10), a compensator for making up for electromagnetic non-linearity in the tilt loops is designed as follows.

$$\begin{cases} u_{cx} = -\dfrac{k_{N0}}{k_{EM0}}\phi_e \\ u_{cz} = -\dfrac{k_{N0}}{k_{EM0}}\varphi_e \end{cases}. \tag{3.5}$$

In (3.5), u_{cx} and u_{cz} are the non-linearity compensator outputs while ϕ_e and φ_e are the non-linearity compensator inputs or the observer outputs.

Next, the performance and robust stability of the AMFC method will be analyzed in Chapter 4, and simulation results of the AMFC method will be introduced in Chapter 5.

4 PERFORMANCE, STABILITY AND ROBUSTNESS ANALYSIS

In this section, under the assumption of linear and time-invariant system, the convergence of AMF-AVS observer, gain characteristics from the sensor noise input to the control command output, and the steady state error of the tilt loops are analyzed first. Then considering the adaptive mechanism of AMFC-AVS, the closed-loop stability and robustness are analyzed.

4.1 PERFORMANCE ANALYSIS

Considering the AMFC shown in Fig. 3.1 and Fig. 3.2, and since the insertion of the non-linearity compensator expressed in (3.5), we can ignore the effect of the non-linearity of electromagnets and think that the transfer function of electromagnets is k_{EM}. Moreover, if gyro-decoupling network works well, the rotor dynamics can be decoupled and can be described by $\frac{1}{J_w s^2}$ in each axis. Under this assumption it is reasonable to analyze the performance of AMFC only in one axis, but the result will be fit for both tilting axes. Denote the sum of all gap-sensor noises is inserted into the closed-loop system from noise input ξ, i.e. ξ_ϕ or ξ_φ which have been defined in (2.13). Without considering the adaptive mechanism of AMF-AVS, suppose that k_{11}, k_{12}, k_{21} and k_{22} are constants, and denote $k_{11}+k_{12}=k_1$ and $k_{12}+k_{22}=k_2$. Furthermore, assume that the controller is simply a PID controller. By such simplifications, Fig. 3.2 can be re-plotted as Fig. 4.1.

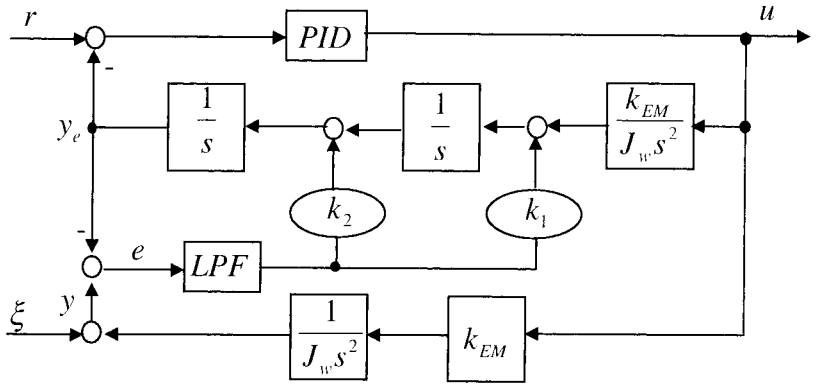

Fig. 4.1 Block diagram of AMFC for system performance analysis

4.1.1 Convergence of AMFC Observer

According to Fig. 4.1, when the convergence of the AMFC observer is studied, we can assume that $\xi = 0$ and ignore the effect of PID controller, then we have the following expressions.

$$e = y - y_e, \tag{4.1}$$

$$y = \frac{k_{EM}}{J_w s^2} u, \tag{4.2}$$

$$y_e = \frac{ak_1}{s^2(s+a)} e + \frac{ak_2}{s(s+a)} e + \frac{k_{EM}}{J_w s^2} u. \tag{4.3}$$

Subsequently, we can obtain the following error equation,

$$(s^3 + as^2 + ak_2 s + ak_1) e = 0. \tag{4.4}$$

For the AMFC observer to be stable, all the poles of (4.4) must fall in the left half plane of s. Then by using Routh criterion of stability, we know that the AMFC observer is stable if $k_2 > k_1/a > 0$. In this case, the error e asymptotically goes to zero as time goes to infinity.

4.1.2 Gain Characteristics from the Sensor Noise Input to the Control Command Output

According to Fig. 4.1, when the gain characteristics from the sensor noise input ξ to the control command output u is considered, we assume that $r = 0$. Then we have the following expressions.

$$u = -F(PID) y_e, \tag{4.5}$$
$$e = y - y_e, \tag{4.6}$$
$$y = \frac{k_{EM}}{J_w s^2} u + \xi, \tag{4.7}$$
$$y_e = \frac{ak_1}{s^2(s+a)} e + \frac{ak_2}{s(s+a)} e + \frac{k_{EM}}{J_w s^2} u. \tag{4.8}$$

Consequently, we obtain the transfer function from the sensor noise input ξ to the control command output u, which is shown as follows.

$$u = \frac{-F(PID) s^2 (ak_2 s + ak_1)}{(s^3 + as^2 + ak_2 s + ak_1)\left(s^2 + \frac{k_{EM}}{J_w} F(PID)\right)} \xi \tag{4.9}$$

According to (4.9), we know that the design of observer represented by characteristic polynomial $s^3 + as^2 + ak_2 s + ak_1$ is independent of the design of controller expressed by characteristic polynomial $s^2 + \frac{k_{EM}}{J_w} F(PID)$. Therefore, in order to satisfy the requirement of sensor noise suppression, it is easy to design k_1 and k_2 under the loose condition $k_2 > k_1/a > 0$.

Since k_2 is a proportional coefficient of the rate input of the observer, k_2 obviously affects the cut-off frequency of the gain characteristics from ξ to u. Increasing k_2, the bandwidth of the gain characteristics will increase greatly. Decreasing k_2, the convergence of the observer may become slow.

Compared with k_2, k_1 has less effect on the frequency response from ξ to u,but it affects the convergence of the observer by affecting the poles of the observer. Increasing k_1,the poles near the imaginary axis will shift to the left , while the poles far from the imaginary axis will shift to the right.

Therefore, we can choose k_1 and k_2 in the following way. First set $k_1 = 1$ and select k_2 according to the requirements of vibration suppression and the convergence speed of the observer. Then adjust k_1 according to the poles of the observer.

Based on the above design steps, we choose $k_1 = 1$ and $k_2 = 2$. Fig. 4.2 shows the gain characteristics from ξ to u when $k_1 = 1$ and $k_2 = 2$. For comparison, the gain characteristics from ξ to u when $k_1 = 10$, $k_2 = 10$, and $k_1 = 20$, $k_2 = 10$ are shown in Fig.4.3. It is easy to see that the gain decreases by 20 dB/decade in higher frequency region.

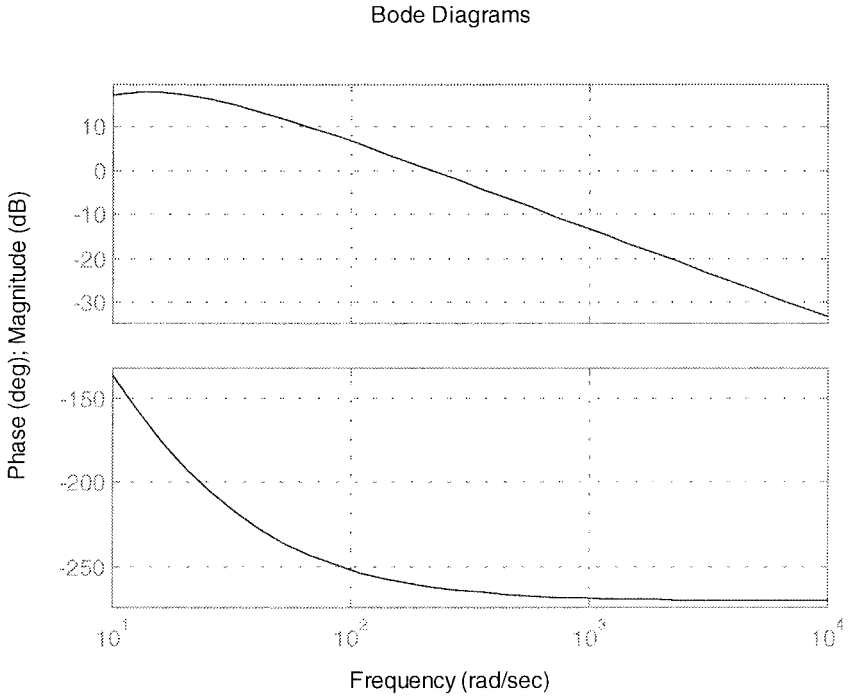

Fig. 4.2 Gain characteristics from sensor noise input ξ to control command output u when $k_1 = 1$ and $k_2 = 2$

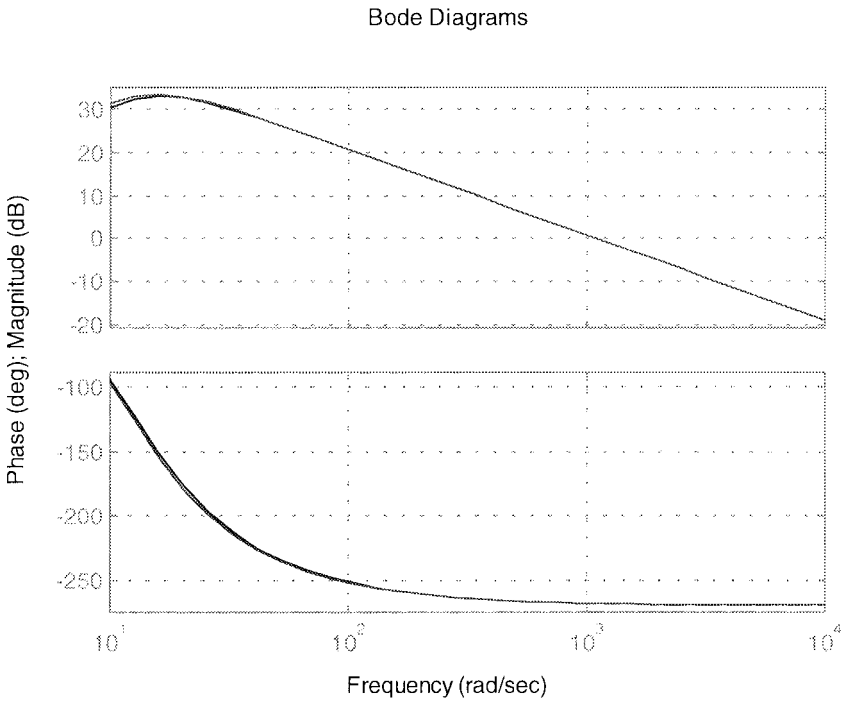

Fig. 4.3 Gain characteristics from sensor noise input ξ to control command output u when $k_1 = 10$, $k_2 = 10$, and $k_1 = 20$, $k_2 = 10$

4.1.3 Steady State Error of the Tilt Loops

According to Fig. 4.1 and assuming $\xi = 0$, we have the following expressions.

$$y = \frac{k_{EM}}{J_w s^2} F(PID)(r - y_e), \tag{4.10}$$

$$y_e = \frac{ak_1}{s^2(s+a)}(y - y_e) + \frac{ak_2}{s(s+a)}(y - y_e) + \frac{k_{EM}}{J_w s^2} F(PID)(r - y_e). \tag{4.11}$$

Then we obtain

$$r - y = \frac{1}{1 + \frac{k_{EM}}{J_w s^2} F(PID)} r. \tag{4.12}$$

(4.12) shows that AMFC can realize zero-error tracking in tilt loops for ramp and step command input.

4.2 Stability and Robustness of the Closed-loop System

According to Chapter 2 and Chapter 3, we know that the closed-loop system containing the plant to be controlled, i.e. MBMW itself, and AMFC's control loop is non-linear and time varying. Therefore, the following robust-stability analysis follows an engineering approach. In this section, first the closed-loop transfer function of the MBMW control system is derived under the as-

sumption that k_{11}, k_{12}, k_{21} and k_{22} are constants and the controller is simply a PID controller. Then the robust-stability of the closed-loop system is analyzed by considering the adaptive mechanism of AMF-AVS.

4.2.1 closed-loop transfer function of the MBMW control system

According to Chapter 2 and Chapter 3, assuming that $T_{dx} = 0$, $T_{dz} = 0$, and position commands are zero, and neglecting the attitude motion of spacecraft, then we have the following mathematical expressions of MBMW and the AMFC loop.

(1) Wheel Dynamics

$$\begin{cases} \ddot{\phi}_w - \sigma\Omega\dot{\varphi}_w = T'_{wx}/J_w \\ \ddot{\varphi}_w + \sigma\Omega\dot{\phi}_w = T'_{wz}/J_w \end{cases}. \tag{4.13}$$

(2) Electromagnets

$$\begin{cases} T'_{wx} = k_{EM}\, v_\phi + k_N \phi_w \\ T'_{wz} = k_{EM}\, v_\varphi + k_N \varphi_w \end{cases}. \tag{4.14}$$

(3) Gap Sensors

$$\begin{cases} \tilde{\phi}_w = \phi_w + \xi_\phi \\ \tilde{\varphi}_w = \varphi_w + \xi_\varphi \end{cases}. \tag{4.15}$$

(4) Observer

$$\begin{cases} \phi_e = \left[\dfrac{a(k_{11}+k_{21})}{s^2(s+a)} + \dfrac{a(k_{12}+k_{22})}{s(s+a)}\right](\tilde{\phi} - \phi_e) + \dfrac{k_{EM0}}{J_{w0}s^2}u_x \\ \varphi_e = \left[\dfrac{a(k_{11}+k_{21})}{s^2(s+a)} + \dfrac{a(k_{12}+k_{22})}{s(s+a)}\right](\tilde{\varphi} - \varphi_e) + \dfrac{k_{EM0}}{J_{w0}s^2}u_z \end{cases}. \tag{4.16}$$

(5) Nutation Damping

$$\begin{cases} u_{nx} = -\dfrac{k_{nut}}{k_{EM0}} J_{wy0}\Omega_0 \dfrac{\kappa s^2}{s^2 + \kappa s + (\sigma_0\Omega_0)^2} \cdot \dfrac{b}{s+b}\tilde{\varphi}_w \\ u_{nz} = -\dfrac{k_{nut}}{k_{EM0}} J_{wy0}\Omega_0 \dfrac{\kappa s^2}{s^2 + \kappa s + (\sigma_0\Omega_0)^2} \cdot \dfrac{b}{s+b}\tilde{\phi}_w \end{cases}. \tag{4.17}$$

(6) Non-linearity Compensator

$$\begin{cases} u_{cx} = -\dfrac{k_{N0}}{k_{EM0}}\phi_e \\ u_{cz} = -\dfrac{k_{N0}}{k_{EM0}}\varphi_e \end{cases}. \tag{4.18}$$

(7) Gyro-decoupling Network

$$\begin{cases} u_{gx} = -\sigma_0 \Omega_0 \dfrac{1}{s} u_z \\ u_{gz} = \sigma_0 \Omega_0 \dfrac{1}{s} u_x \end{cases} . \tag{4.19}$$

(8) PID Controller

$$\begin{cases} u_x = -(k_p + \dfrac{k_i}{s} + k_d s)\phi_e \\ u_z = -(k_p + \dfrac{k_i}{s} + k_d s)\varphi_e \end{cases} . \tag{4.20}$$

(9) Total Control

$$\begin{cases} v_\phi = \dfrac{1}{\tau s + 1}(u_x + u_{gx} + u_{cx} + u_{nx}) \\ v_\varphi = \dfrac{1}{\tau s + 1}(u_z + u_{gz} + u_{cz} + u_{nz}) \end{cases} . \tag{4.21}$$

Where τ is time delay, which is caused by electronic circuits and electromagnets.
According to (4.13)～(4.21), we can derive the following closed-loop transfer function.

$$\begin{cases} \phi = \dfrac{k_{EM}}{J_w} \dfrac{F_{11}G_{22} - F_{21}G_{12}}{G_{11}G_{22} - G_{12}G_{21}} \xi_\phi + \dfrac{k_{EM}}{J_w} \dfrac{F_{12}G_{22} - F_{22}G_{12}}{G_{11}G_{22} - G_{12}G_{21}} \xi_\varphi \\ \varphi = \dfrac{k_{EM}}{J_w} \dfrac{F_{21}G_{11} - F_{11}G_{21}}{G_{11}G_{22} - G_{12}G_{21}} \xi_\phi + \dfrac{k_{EM}}{J_w} \dfrac{F_{22}G_{11} - F_{12}G_{21}}{G_{11}G_{22} - G_{12}G_{21}} \xi_\varphi \end{cases} . \tag{4.22}$$

In (4.22),

$$\begin{bmatrix} F_{11} & F_{12} \\ F_{21} & F_{22} \end{bmatrix} = \begin{bmatrix} -\left(F(PID) + \dfrac{k_{N0}}{k_{EM0}}\right)\dfrac{B}{A} & \sigma_0 \Omega_0 \dfrac{1}{s} \cdot \dfrac{B}{A} F(PID) - \dfrac{D}{C} \\ -\sigma_0 \Omega_0 \dfrac{1}{s} \cdot \dfrac{B}{A} F(PID) + \dfrac{D}{C} & -\left(F(PID) + \dfrac{k_{N0}}{k_{EM0}}\right)\dfrac{B}{A} \end{bmatrix},$$

$$\begin{bmatrix} G_{11} & G_{12} \\ G_{21} & G_{22} \end{bmatrix} = \begin{bmatrix} \left(s^2 - \dfrac{k_N}{J_w}\right)(\tau s + 1) - \dfrac{k_{EM}}{J_w} F_{11} & -\sigma \Omega s(\tau s + 1) - \dfrac{k_{EM}}{J_w} F_{12} \\ \sigma \Omega s(\tau s + 1) - \dfrac{k_{EM}}{J_w} F_{21} & \left(s^2 - \dfrac{k_N}{J_w}\right)(\tau s + 1) - \dfrac{k_{EM}}{J_w} F_{22} \end{bmatrix},$$

$$\frac{B}{A} = \frac{a(k_{12} + k_{22})s + a(k_{11} + k_{21})}{s^3 + as^2 + a(k_{12} + k_{22})s + a(k_{11} + k_{21}) + (s + a)F(PID)\dfrac{k_{EM0}}{J_{w0}}},$$

$$\frac{D}{C} = \frac{k_{nut}}{k_{EM0}} J_{wy0} \Omega_0 \frac{\kappa s^2}{s^2 + \kappa s + (\sigma_0 \Omega_0)^2} \cdot \frac{b}{s + b},$$

$$F(PID) = k_p + \frac{k_i}{s} + k_d s .$$

4.2.2 Robust Stability

In the following, we discuss and analyze the robust stability of proposed control system from engineering viewpoint. It should be noted, however, that the discussion does not offer a rigorous proof of the robust stability.

The AMFC only has its observer adaptively switched between two groups of parameters. One group of parameters is $[k_{11}\ k_{12}\ k_{21\_off}\ k_{22\_off}]\triangleq \boldsymbol{K}_1$, the other group of parameters is $[k_{11}\ k_{12}\ k_{21\_on}\ k_{22\_on}]\triangleq \boldsymbol{K}_2$. If characteristic variable $|y\_ave|$ is larger than a steady-state threshold δ_1 and smaller than a saturation threshold δ_2, then $\boldsymbol{K}_2$ is switched on as observer parameters, otherwise $\boldsymbol{K}_1$ is switched on. Since y_ave is the average value of y_lpf in one wheel rotational period, then y_lpf can be expressed as $y\_lpf \approx y\_ave + f(\Omega, 2\ \Omega, \cdots)$, where $\Omega = 2\pi/T_w$ and T_w is wheel rotational period. Suppose that both the closed-loop system containing $\boldsymbol{K}_1$ and the closed-loop system containing $\boldsymbol{K}_2$ are asymptotically stable. Define area $\mathrm{I} = \{y\_ave \,|\, |y\_ave| \le \delta_1\}$, area $II = \{y\_ave \,|\, \delta_1 < |y\_ave| < \delta_2\}$, and area $III = \{y\_ave \,|\, |y\_ave| \ge \delta_2\}$. Since $\delta_1 \ll \delta_2$, then the stability analysis in area I, II, and III can be carried on equivalently and separately in area I and II, and in area II and III. First consider the stability in area I and II. If at time $N_1 T_w$ (N_1 is an integer), $|y\_ave| > \delta_1$ and $\boldsymbol{K}_2$ is switched on, then an integer $N_2\,(N_2 > N_1)$ must exist so that at time $N_2 T_w$, $|y\_ave| \le \delta_1$, and the observer parameters are switched to $\boldsymbol{K}_1$. From time $N_2 T_w$, if $|y\_ave|$ keeps smaller than δ_1, then it will converge to zero and the amplitude of f (Ω, 2 $\Omega\cdots$) will converge too. After time $N_2 T_w$, if $|y\_ave|$ is larger than δ_1 again, then it must become smaller at another time $N_3 T_w$ ($N_3 > N_2$, N_3 is an integer). If $\boldsymbol{K}_1$ and $\boldsymbol{K}_2$ are designed suitably, then after several times switches, the closed-loop system will converge to steady state. By the same kind of discussion, the stability in area II and III can also be analyzed if the saturation nonlinearity does not make system unstable. As a result, if $\boldsymbol{K}_1$, $\boldsymbol{K}_2$, δ_1, δ_2 and controller are designed reasonably, after finite times of switches the closed-loop system will enter steady state. In simulation, only one to three times switches occurred.

According to the transfer function of the closed-loop system shown in (4.22), the asymptotic stability and robust-stability of the closed-loop system including $\boldsymbol{K}_1$ and those of the closed-loop system including $\boldsymbol{K}_2$ are analyzed separately. For the MBMW whose parameters are listed in Table 4.1, and the AMFC's control loop whose parameters are as listed in Table 4.2, the robust stability range of J_w, k_{EM}, $k_{N\phi}$, $k_{N\varphi}$, Ω, and σ as a whole, i.e. $[J_w/J_{w0}\ k_{EM}/k_{EM0}\ k_{N\phi}/k_{N\phi0}\ k_{N\phi}/k_{N\varphi0}\ \Omega/\Omega_0\ \sigma/\sigma_0] = \Sigma/\Sigma_0[1\ 1\ 1\ 1\ 1\ 1]$, is demonstrated in Table 4.3. Considering the time delay in electromagnets, which is modeled as $\frac{1}{\tau s+1}$, where τ is time constant and $\tau = 0.01$, the robust-stability range of J_w, k_{EM}, $k_{N\phi}$, $k_{N\varphi}$, Ω, and σ as a whole is demonstrated in Table 4.4.

For case H and case G in Table 4.3, the root loci of the closed-loop system with respect to Σ/Σ_0, J_w/J_{w0}, σ/σ_0, $k_{N\phi}/k_{N\phi0}$, $k_{N\varphi}$, and Ω/Ω_0 are demonstrated in Fig. 4.4〜Fig. 4.9, respectively. In Fig. 4.4〜Fig. 4.9, asterisks show the positions of the poles of the closed-loop system when J_w, k_{EM}, $k_{N\phi}$, $k_{N\varphi}$, Ω, and σ reach their nominal values, i.e. $\Sigma/\Sigma_0 = 1$.

Table 4.1 parameters of MBMW

J_w	σ	k_{EM}	$k_{N\phi}\,(k_{N\varphi})$	V_b	N_s	ϕ_g	φ_g	c_1, c_3, c_5	c_2, c_4, c_6
0.0129 kgm^2	1.85	0.0448 Nm/V	3.4225 Nm	0.8 V	6	0.6 deg	0.6 deg	0.004 deg	0.0005 deg

Table 4.2 parameters of AMFC

$\varkappa$	b	$k_p gain$	$k_i gain$	$k_d gain$	k_{11}	k_{12}	k_{21}	k_{22}	a	k_{nut}	k_{logic}	δ_1	δ_2
32	10	121.2	150	15.64	1	2	0/20	0/5	25	k_{EM0}	5	10^{-5}	0.0035

Table 4.3 robust stability range of AMFC when $\tau = 0$ sec

Case	k_{11}	k_{12}	k_{21}	k_{22}	σ	r(rpm)	Σ/Σ_0
A	1	2	20	5	1.6	1000	0.7～1.24
B	↓	↓	↓	↓	↓	6000	0.6～1.25
C	↓	↓	↓	↓	1.85	1000	0.7～1.24
D	↓	↓	↓	↓	↓	6000	0.6～1.25
E	↓	↓	0	0	1.6	1000	0.6～1.47
F	↓	↓	↓	↓	↓	6000	0.4～1.47
G	↓	↓	↓	↓	1.85	1000	0.5～1.47
H	↓	↓	↓	↓	↓	6000	0.4～1.47

Table 4.4 robust stability range of AMFC when τ=0.01 sec

case	A	B	C	D	E	F	G	H
Σ/Σ_0	0.7～1.03	0.6～1.0	0.7～1.02	0.6～1.0	0.6～1.03	0.4～1.0	0.6～1.02	0.4～1.0

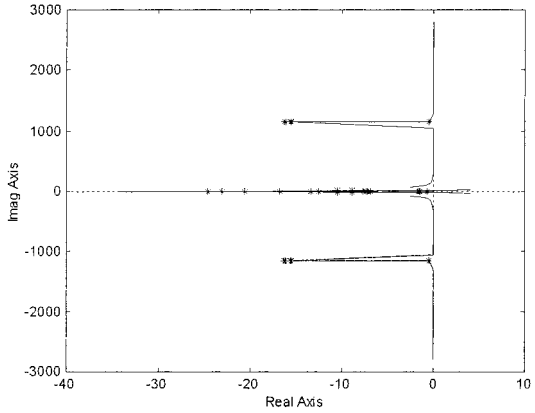

Fig. 4.4 Root locus of the closed-loop system with respect to Σ/Σ_0
(case H, $\Sigma/\Sigma_0 \in [0.25,\ 1.55]$)
(critical points: Σ/Σ_0= 0.34, 1.47)

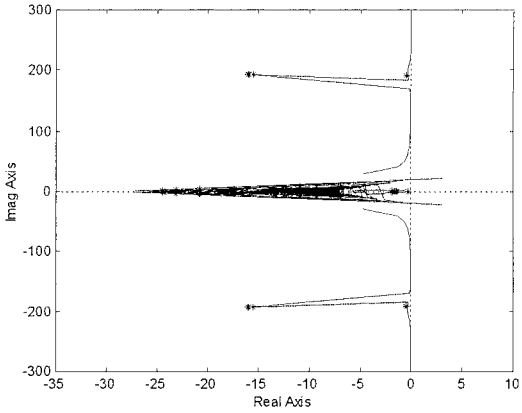

Fig. 4.5 Root locus of the closed-loop system with respect to Σ/Σ_0
(case G, $\Sigma/\Sigma_0 \in [0.46,\ 1.54]$)
(critical points: Σ/Σ_0= 0.49, 1.47)

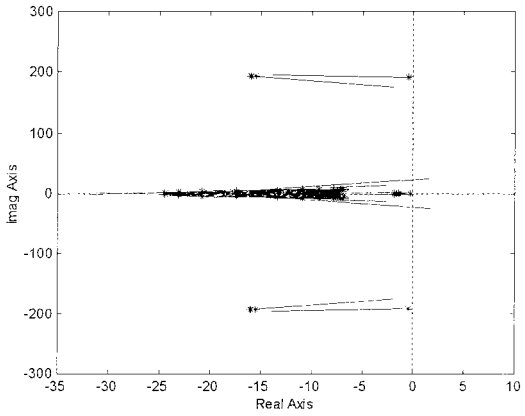

Fig. 4.6 Root locus of the closed-loop system with respect to J_w/J_{w0}
(case G, $J_w/J_{w0} \in [0.1,\ 2700]$)
(critical points: J_w/J_{w0}= 0.16, 7×10^9)

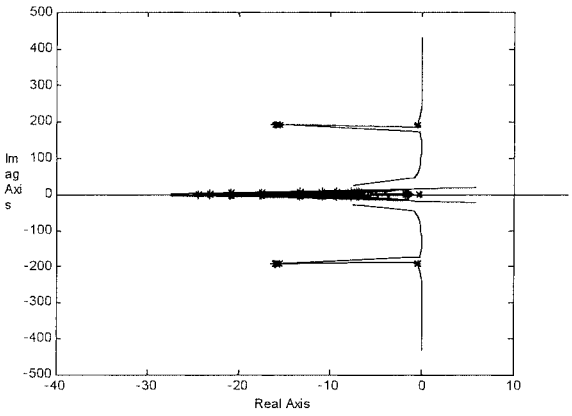

Fig. 4.7 Root locus of the closed-loop system with respect to σ/σ_0
(case G, $\sigma/\sigma_0 \in [0.2,\ 2.23]$)
(critical points: σ/σ_0= 0.24, 2.16)

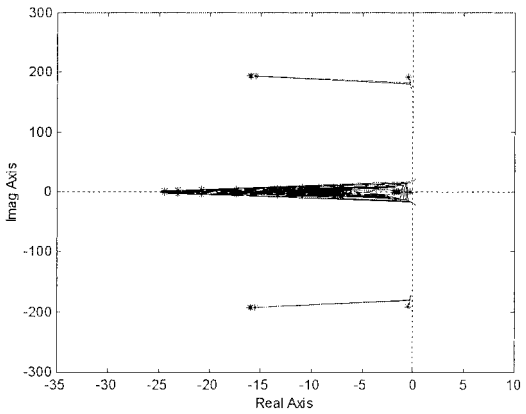

Fig. 4.8 Root locus of the closed-loop system with respect to $k_{N\phi}/k_{N\phi 0}$ and $k_{N\varphi}/k_{N\varphi 0}$ (case G, $k_{N\phi}/k_{N\phi 0} = k_{N\varphi}/k_{N\varphi 0} \in [0, 14]$) (critical points: $k_{N\phi}/k_{N\phi 0}$=$k_{N\varphi}/k_{N\varphi 0}$=0, 11)

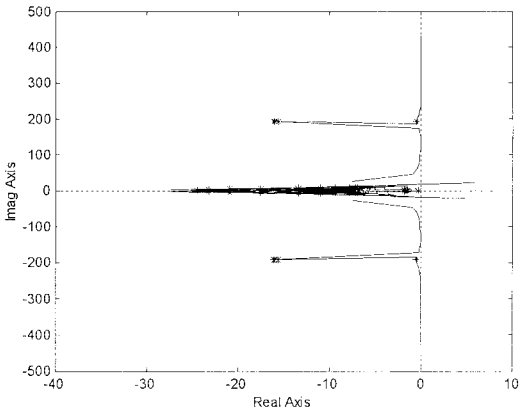

Fig. 4.9 Root locus of the closed-loop system with respect to Ω/Ω_0 (case G, $\Omega/\Omega_0 \in [0.2, 2.23]$) (critical points: Ω/Ω_0= 0.24, 2.16)

5 SIMULATION OF THE ACTIVE CONTROL OF MBMW

The active control of MBMW by using AMFC method is simulated numerically by using C language. In this Chapter a MBMW is selected as an example for system simulation, although the AMFC method can be easily applied to the active control of other MBMW. Continuous system simulation is executed by selecting 0.1 msec as sampling period. In this Chapter first simulation results for normal case in comparison with other methods are illustrated. Then, the simulation results considering that parameters are uncertain and sensor noises are strengthened are demonstrated.

5.1 NORMAL CASE

In normal case, the AMFC method, MFC method [2], and H_∞ control method [1] are simulated for comparison. Both AMFC and MFC use the same kind of non-linearity compensator proposed in this report. The parameters of AMFC's control loop are as listed in Table 4.2. MFC has the same parameters as AMFC except for adaptive mechanism, logical derivative and nutation damping. The H_∞ controller is an eighth-order controller. The parameters of MBMW are listed in Table 4.1. The characteristics of electromagnetic non-linearity are shown in Fig. 2.3. In simulation, a step externally impressed disturbance torque whose amplitude is 0.0005 Nm is inserted in φ_w channel. The simulation results are shown in Fig. 5.1(a, b)〜Fig. 5.8(a, b).

Fig. 5.1(a, b) and Fig. 5.3(a, b) show the true values of the gimballing angles when MFC control method is used and when the wheel rotational speed is 1000 rpm and 6000 rpm, respectively. Fig. 5.2(a, b) and Fig. 5.4(a, b) show the true values of the gimballing angles when AMFC control method is used and when the wheel rotational speed is 1000 rpm and 6000 rpm, respectively. In Fig. 5.1(a, b)〜Fig. 5.4(a, b), (a) and (b) are simulation results when position commands are $\pm$0.005 degree and$\pm$0.1 degree, respectively. Fig. 5.5(a, b) show the true values of the gimballing

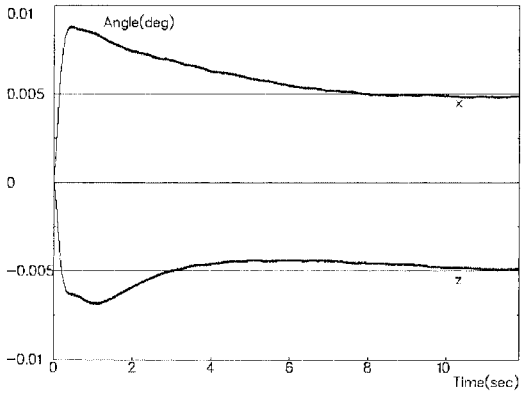

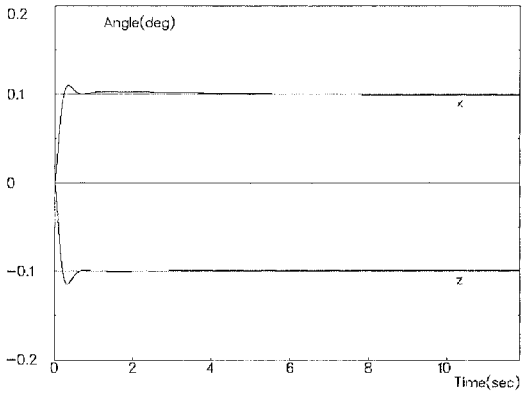

(a) when position commands are $\pm$0.005 deg (b) when position commands are $\pm$0.1 deg

Fig. 5.1 Simulation results of MFC method (1000 rpm)

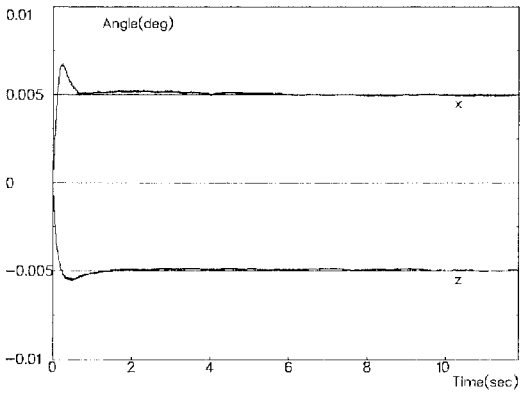

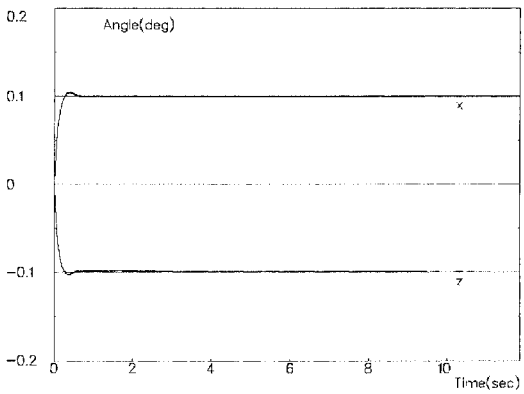

(a) when position commands are $\pm$0.005 deg (b) when position commands are $\pm$0.1 deg

Fig. 5.2 Simulation results of AMFC method (1000 rpm)

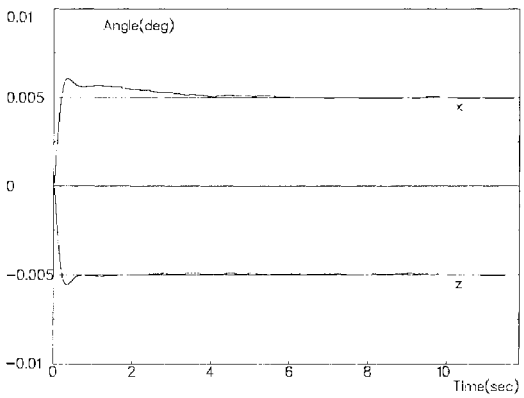

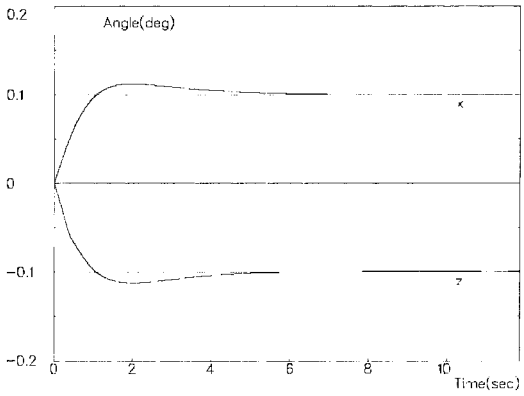

(a) when position commands are $\pm$0.005 deg (b) when position commands are $\pm$0.1 deg

Fig. 5.3 Simulation results of MFC method (6000 rpm)

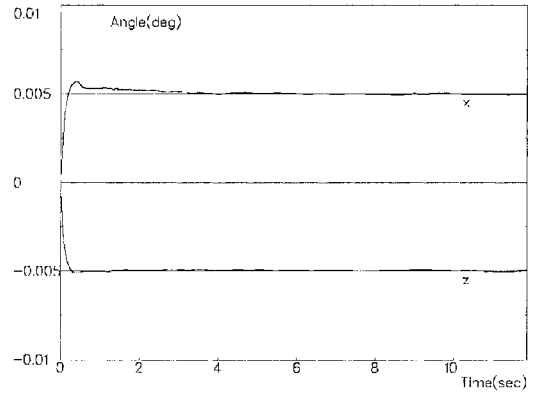

(a) when position commands are±0.005 deg

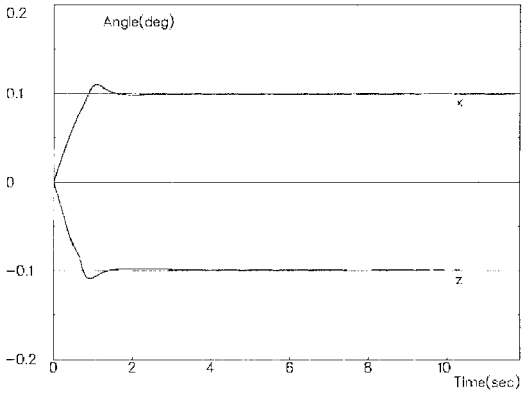

(b) when position commands are ±0.1 deg

Fig. 5.4 Simulation results of AMFC method (6000 rpm)

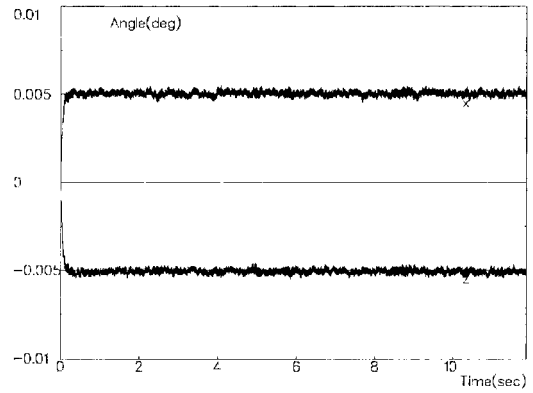

(a) true values of gimballing angles

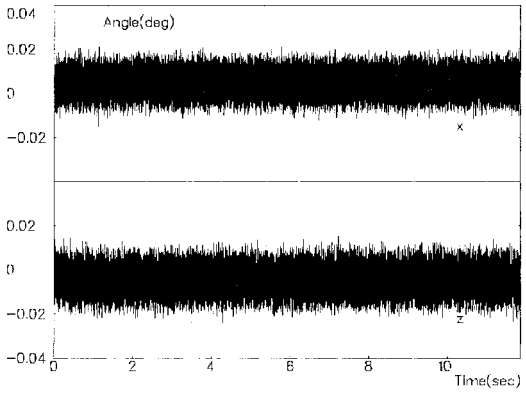

(b) gap sensor outputs of gimballing angles

Fig. 5.5 Simulation results of H_∞ control method (4000 rpm)

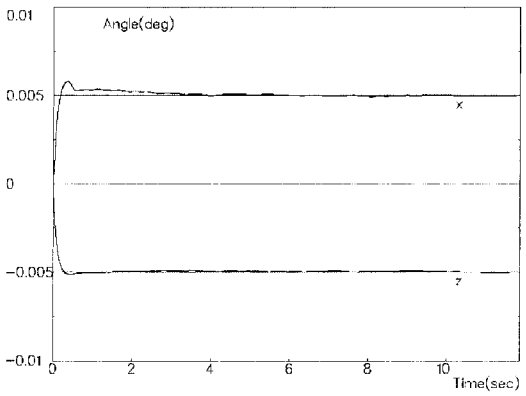

(a) true values of gimballing angles

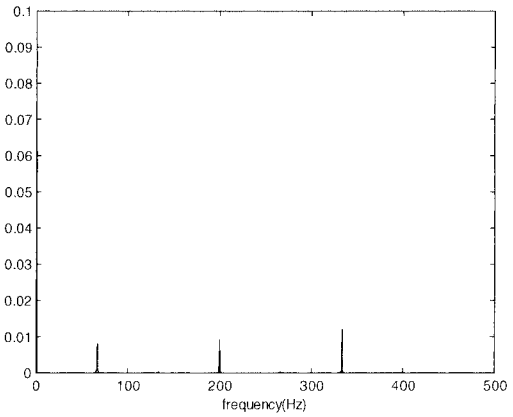

(b) FFT of gap sensor outputs of gimballing angles

Fig. 5.6 Simulation results of AMFC method (4000 rpm)

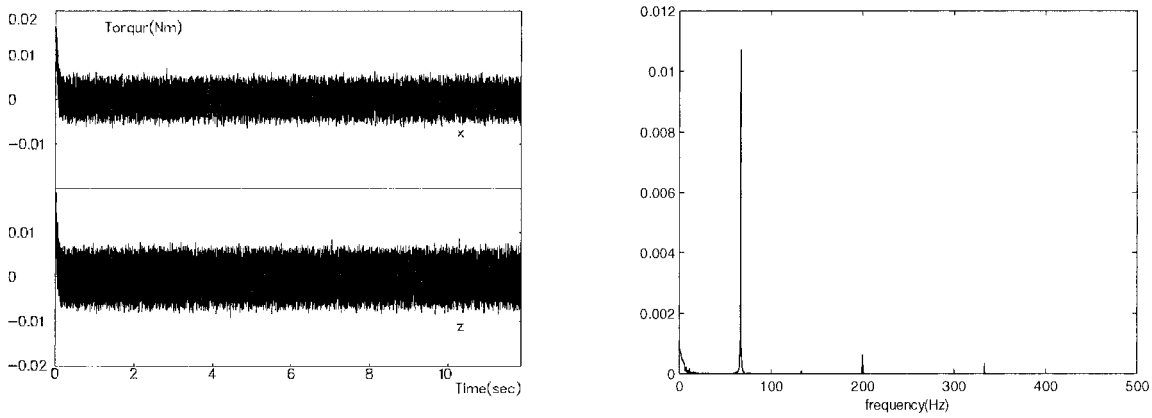

(a) total control torque (b) FFT of total control torque

Fig. 5.7 Simulation results of H_∞ control method (4000 rpm)

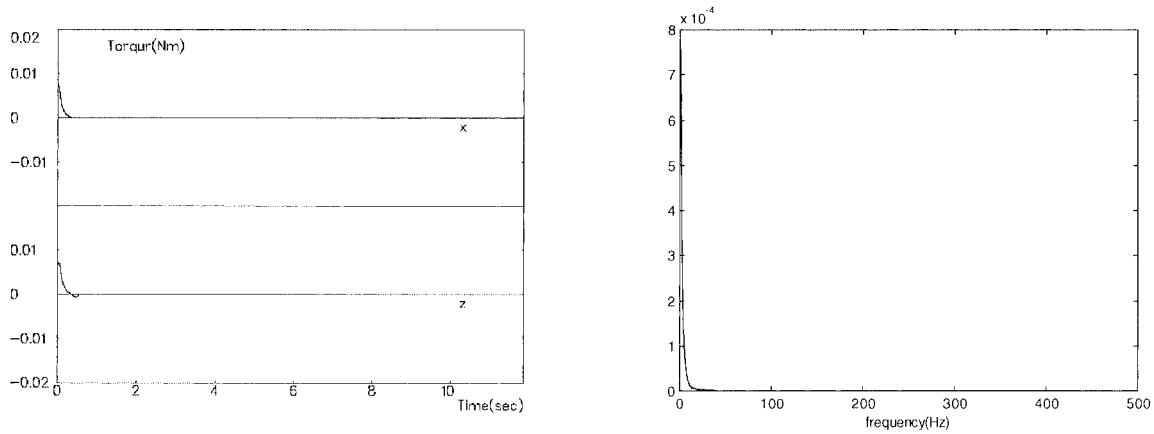

(a) total control torque (b) FFT of total control torque

Fig. 5.8 Simulation results of AMFC method (4000 rpm)

angles and the gap sensor outputs of the gimballing angles when H_∞ control method is used and when the wheel rotational speed is 4000 rpm. Fig. 5.6(a, b) show the true values of the gimballing angles and the Fourier transformation of the gap sensor outputs of the gimballing angles when AMFC control method is used and when the wheel rotational speed is 4000 rpm. Since the same kinds of sensor errors are considered in simulation, according to Fig. 5.5(b) and Fig. 5.6(b), we can have a look of the characteristics of the gap sensor noises and harmonic disturbances in both time domain and frequency domain. Fig. 5.7(a, b) and Fig. 5.8(a, b) show the total control torque and their Fourier transformation when H_∞ control method and AMFC control method are used, respectively.

Simulation results show that both AMFC method and MFC method are robust against wheel rotational speed in a large range and have much better active-vibration suppression compared with H_∞ control method, although by using H_∞ control method almost no overshoot occurs. However, compared with MFC method, AMFC method keeps much smaller overshoot and shorter settling time for different wheel rotational speed and different position commands. Simulation results also show that the new nutation damping method is much effective for a large range of wheel rotational speed. In addition, if a smaller $\varkappa$ can be chosen in practical digital controller design, better

nutation damping can be obtained. The reason is that a smaller $\varkappa$ results in a narrow bandwidth filter in nutation damping loop and accordingly better disturbance suppression in this loop. But if $\varkappa$ is too small, the bandwidth filter of the nutation damping loop is not easy to be realized by using analog circuit in practice.

5.2 ROBUSTNESS AGAINST PARAMETER UNCERTAINTIES

The AMFC method is simulated when parameter J_w, J_{yw}, k_{EM} and k_N are $\pm$20% uncertain while the AMFC loop keeps the same as that of the normal case. The simulation results of the true gimballing angles of MBMW when the wheel rotational speed is 1000 rpm and 6000 rmp are shown in Fig. 5.9 (a, b)〜Fig. 5.14 (a, b), respectively. In simulation externally impressed disturbance torque which is the same as that in section 5.1 is inserted.

Simulation results show that even when parameter J_w, J_{yw}, k_{EM} and k_N have $\pm$20% uncertainties, the AMFC method can still make the closed-loop system stable, and the parameter uncertainties deteriorate system response only a little. Accordingly we can say that the AMFC method is robust against parameter uncertainties.

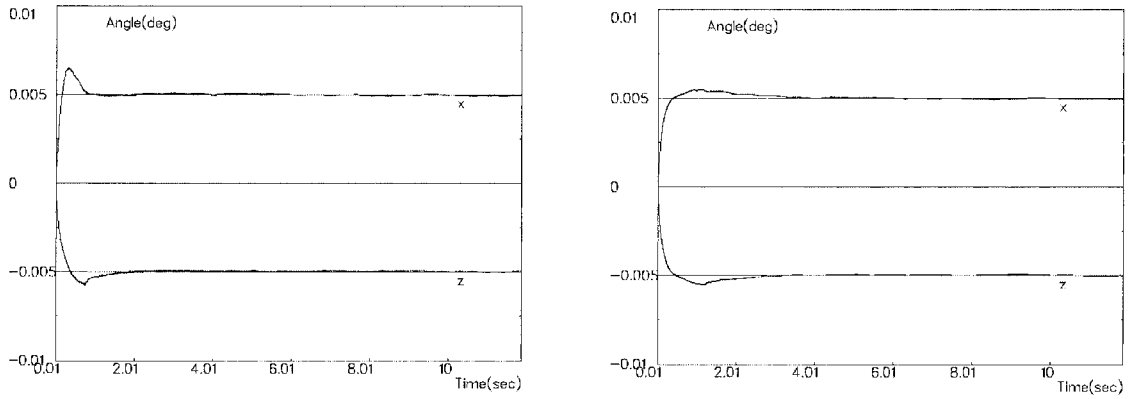

(a) true values of gimballing angles (1000 rpm) (b) true values of gimballing angles (6000 rpm)

Fig. 5.9 Simulation results when J_w and J_{yw} are +20% uncertain

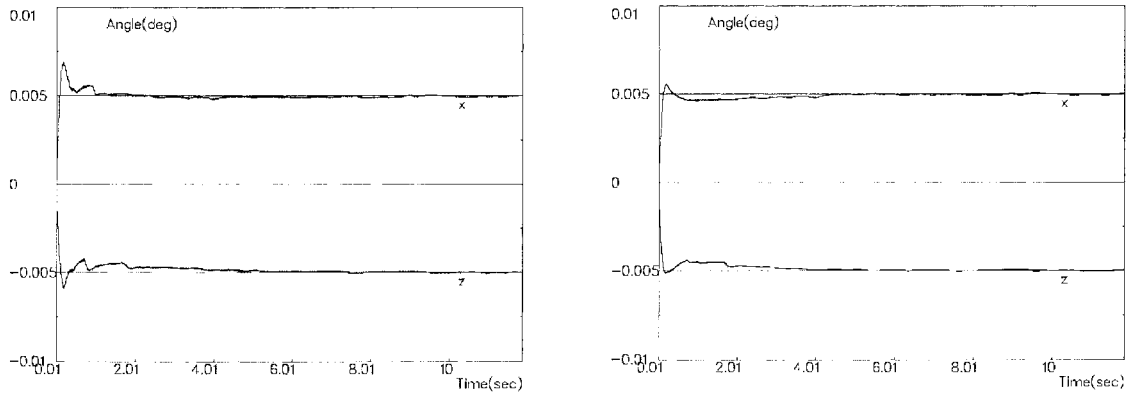

(a) true values of gimballing angles (1000 rpm) (b) true values of gimballing angles (6000 rpm)

Fig. 5.10 Simulation results when J_w and J_{yw} are −20% uncertain

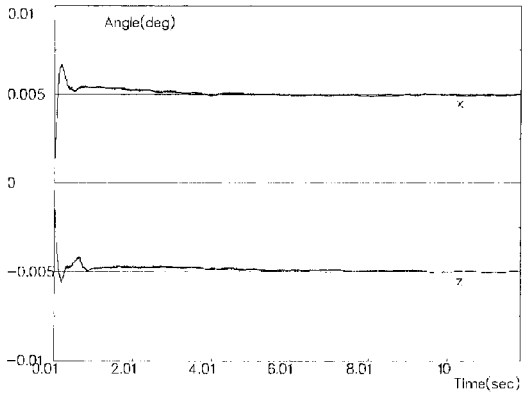

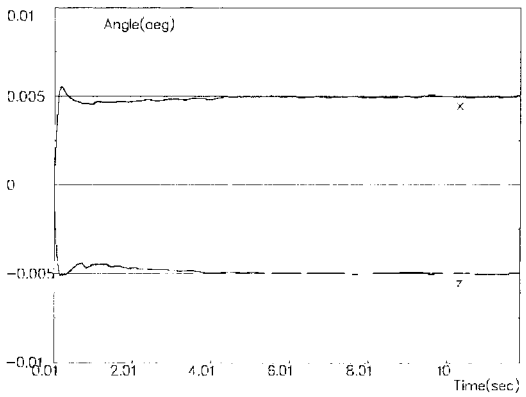

(a) true values of gimballing angles (1000 rpm) (b) true values of gimballing angles (6000 rpm)

Fig. 5.11 Simulation results when k_{EM} are +20% uncertain

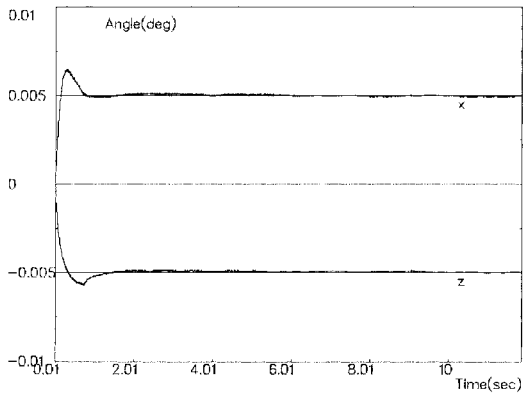

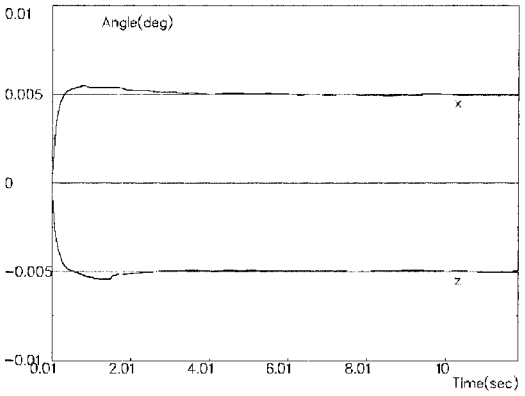

(a) true values of gimballing angles (1000 rpm) (b) true values of gimballing angles (6000 rpm)

Fig. 5.12 Simulation results when k_{EM} are -20% uncertain

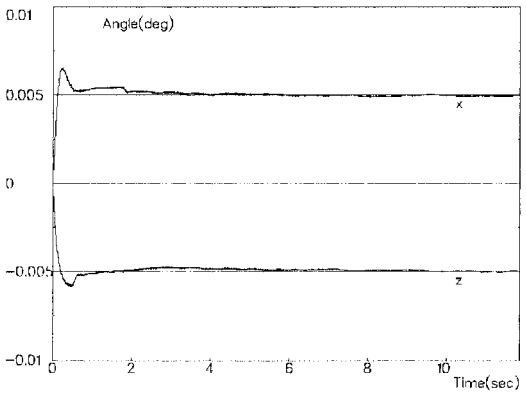

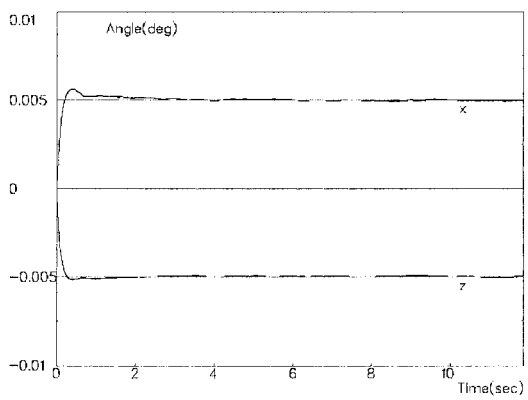

(a) true values of gimballing angles (1000 rpm) (b) true values of gimballing angles (6000 rpm)

Fig. 5.13 Simulation results when k_N are +20% uncertain

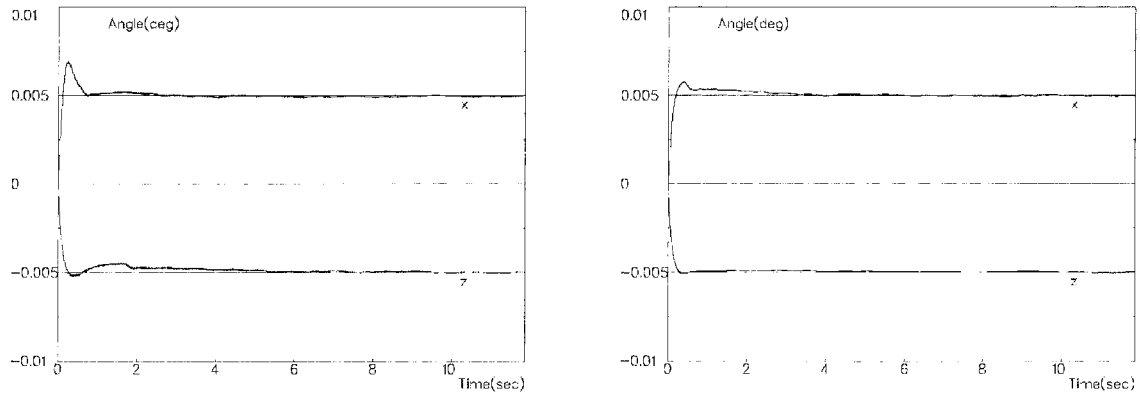

(a) true values of gimballing angles (1000 rpm) (b) true values of gimballing angles (6000 rpm)

Fig. 5.14 Simulation results when k_N are −20% uncertain

5.3 Effect of Sensor White Noise and Harmonic Sensor Noises on System Response

The AMFC method is simulated when sensor white noises and harmonic sensor noises shown in (2.13) are two times larger than that of the normal case while the AMFC loop keeps the same as that of the normal case. The simulation results of the true gimballing angles of MBMW when the wheel rotational speed is 1000 rpm and 6000 rmp are shown in Fig. 5.15(a, b)〜Fig. 5.16(a, b), respectively. In simulation externally impressed disturbance torque which is the same as that in section 5.1 is inserted.

Simulation results show that the AMFC method has satisfactory active-vibration suppression even when sensor white noises and harmonic sensor noises are two times larger than that of the normal case. Simulation results also show that the active-vibration suppression of the AMFC method is more efficient to suppress harmonic sensor noises than to suppress white noises.

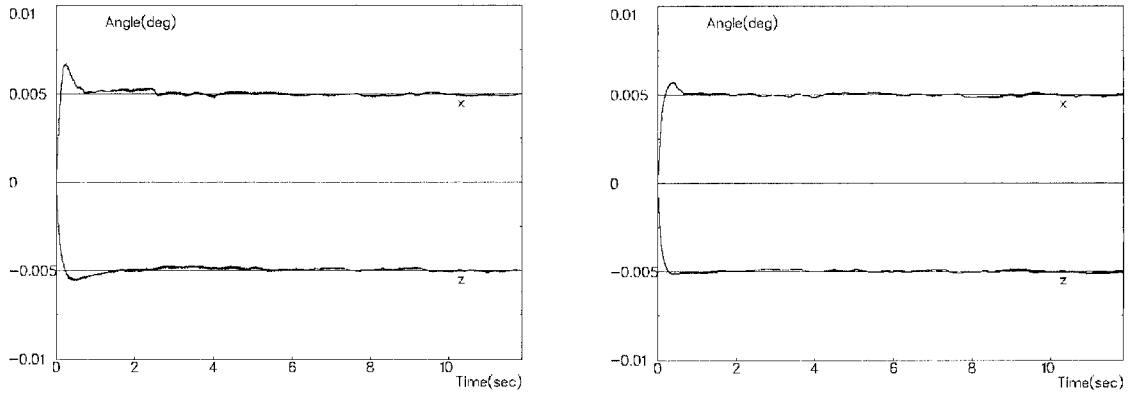

(a) true values of gimballing angles (1000 rpm) (b) true values of gimballing angles (6000 rpm)

Fig. 5.15 Simulation results when sensor white noises are two times larger

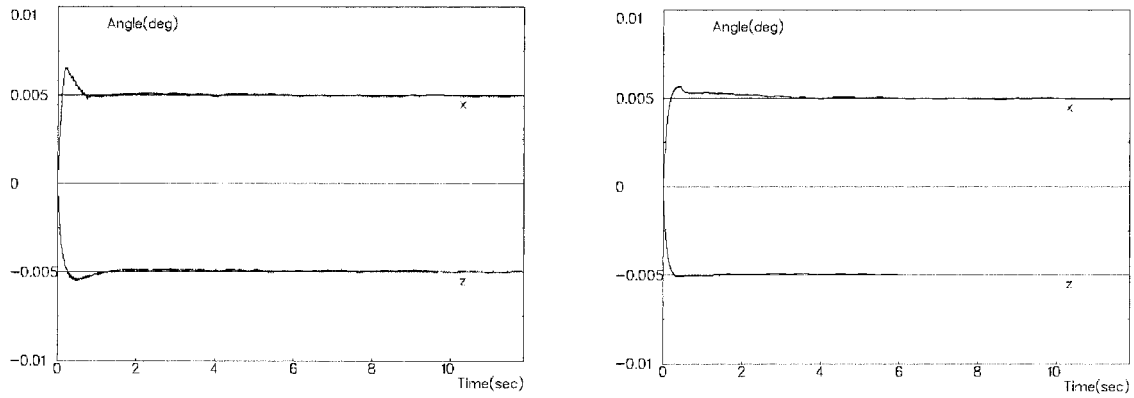

(a) true values of gimballing angles (1000 rpm) (b) true values of gimballing angles (6000 rpm)

Fig. 5.16 Simulation results when harmonic sensor noises are two times larger

5.4 Effect of Sampling Period on System Response

The AMFC method is simulated when sampling period is set as 1 msec while the other conditions are kept the same as that of the normal case. The simulation results of the true gimballing angles of MBMW when the wheel rotational speed is 1000 rpm and 6000 rmp are shown in Fig. 5.17(a, b).

Simulation results show that the AMFC method is robust to sampling period. However, in order to have good active-vibration suppression, sampling period can not be too large.

5.5 Effect of Non-linearity Compensator

The AMFC method is simulated when the ”Non-linearity Compensator” is not used while the other conditions are kept the same as that of the normal case. The simulation results of the true gimballing angles of MBMW when the wheel rotational speed is 1000 rpm and 6000 rmp are

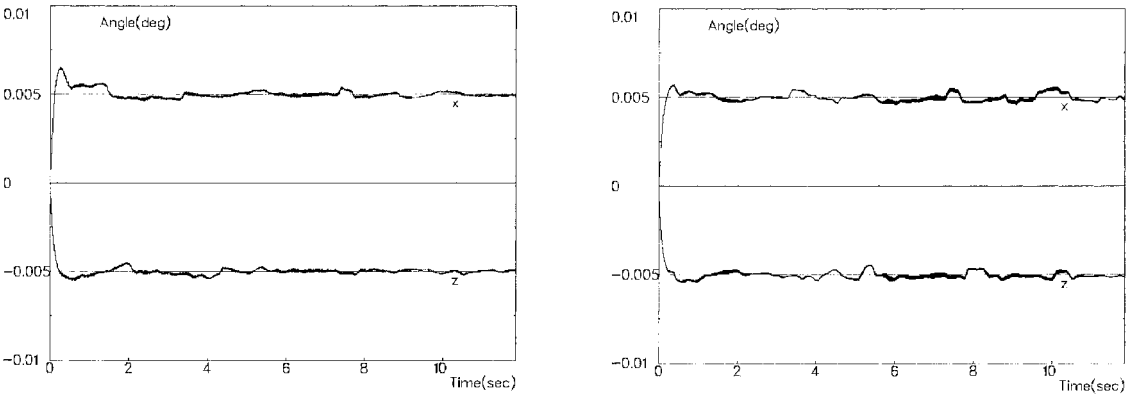

(a) true values of gimballing angles (1000 rpm) (b) true values of gimballing angles (6000 rpm)

Fig. 5.17 Simulation results when sampling period is 1 msec

shown in Fig. 5.18(a, b).

According to Fig. 5.2(b), Fig. 5.4(b) and Fig. 5.18(a, b) we know that when gimballing angle command is large, "Non-linearity Compensator" can improve system dynamic response, especially when the wheel rotational speed is low. The reason is that "Non-linearity Compensator" can generate a control command to cancel or minimize the effect of electromagnetic non-linearity on system dynamic response. The lower the wheel rotational speed is, the greater the effect of electromagnetic non-linearity is, and therefore the clearer the function of the "Non-linearity Compensator" is.

Although in simulation the AMFC method is only applied to a specific MBMW, the AMFC method is easy to be applied to any kind of actively controlled MBMWs. Furthermore, the AMFC method is also easy to be realized in practical engineering. Applying the AMFC method to a prototype actively controlled MBMW owned by ISAS is being considered.

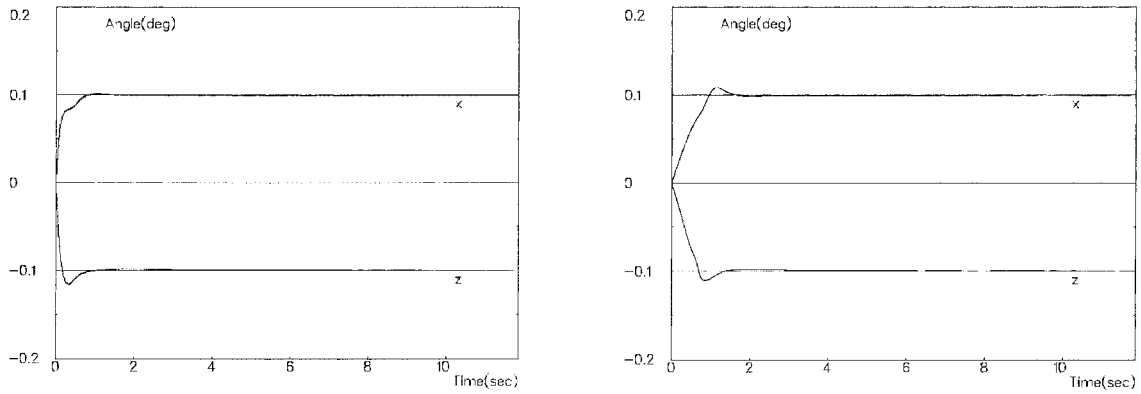

(a) true values of gimballing angles (1000 rpm) (b) true values of gimballing angles (6000 rpm)

Fig. 5.18 Simulation results when "Non-linearity Compensator" is not used

6 SATELLITE ATTITUDE CONTROL BY USING MBMW

For high-accuracy spacecraft attitude control, MBMW has been studied as a promising low noise actuator. In the above Chapters AMFC method is proposed for the active control of MBMW. Study results showed that this method has superior active-vibration suppression, good dynamic response and satisfactory nutation damping for large range of wheel rotational speed. In this Chapter the MBMW controlled by the AMFC method is used as actuator for satellite attitude control.

6.1 SATELLITE ATTITUDE DYNAMICS

In this Chapter a satellite with flexible appendages is studied. In describing the attitude motion of the satellite, rotational coordinate systems are used as shown in Fig. 6.1, in which coordinate system $X_0Y_0Z_0$ is considered as satellite's attitude reference coordinate system while $X_sY_sZ_s$ body-fixed coordinate system. $X_0Y_0Z_0$ changes so slowly in inertial space (in this article, we are tentatively assuming an astronomy mission, such as Solar-A's, although our method can easily be applied to an earth observation mission spacecraft for obtaining a high resolution images) that it can be considered as an inertial coordinate system. Angles ϕ_s, θ_s and φ_s are the Euler angles in X-Z-Y transformation from $X_0Y_0Z_0$ to $X_sY_sZ_s$.

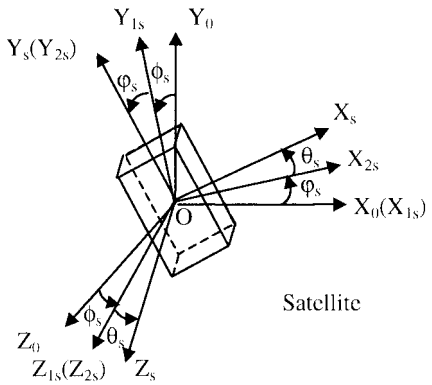

Fig. 6.1 Coordinate systems of satellite

Suppose that the selected coordinates are on the principal axes, the Euler angles of the satellite are small, and the satellite's angular momentum is so small that the coupling between axes can be neglected. Then the linearized dynamic model of the satellite with N_p flexible appendages can be expressed as follows.

$$\begin{cases} \boldsymbol{J}_s \dot{\boldsymbol{\omega}}_s = \boldsymbol{T}_s - \sum_{i=1}^{N_p} \boldsymbol{\delta}_{pi}^T \ddot{\boldsymbol{\eta}}_{pi} \\ \ddot{\boldsymbol{\eta}}_{pi} + \boldsymbol{D}_{pi} \dot{\boldsymbol{\eta}}_{pi} + \boldsymbol{E}_{pi} \boldsymbol{\eta}_{pi} + \boldsymbol{\delta}_{pi} \dot{\boldsymbol{\omega}}_s = 0 \quad (i = 1, 2, \cdots, N_p) \end{cases} . \tag{6.1}$$

In (6.1), $\boldsymbol{J}_s$ is the inertial tensor matrix of the satellite. $\boldsymbol{T}_s$ is the total torque vector working on the satellite. ω_s is the satellite's angular velocity vector. η_{pi} is the flexibility mode vector of the i th flexible appendage. δ_{pi} is the modal conjunction-coefficient matrix. $\boldsymbol{D}_{pi}$ is the modal attenuation-coefficient matrix. $\boldsymbol{E}_{pi}$ is the modal stiffness-coefficient matrix. And

$$\boldsymbol{T}_s = \begin{bmatrix} T_{sx} \\ T_{sy} \\ T_{sz} \end{bmatrix}, \quad \boldsymbol{\omega}_s = \begin{bmatrix} \dot{\phi}_s \\ \dot{\theta}_s \\ \dot{\varphi}_s \end{bmatrix}, \quad \boldsymbol{\eta}_{pi} = \begin{bmatrix} \eta_{1pi} \\ \vdots \\ \eta_{m_{pi}pi} \end{bmatrix}, \quad \boldsymbol{J}_s = \begin{bmatrix} J_{sx} & 0 & 0 \\ 0 & J_{sy} & 0 \\ 0 & 0 & J_{sz} \end{bmatrix}, \quad \boldsymbol{\delta}_{pi} \text{ is } m_{pi} \times 3 \text{ matrix},$$

$$\boldsymbol{D}_{pi} = \begin{bmatrix} 2\rho_{1pi}\omega_{1pi} & & & \\ & 2\rho_{2pi}\omega_{2pi} & & \\ & & \ddots & \\ & & & 2\rho_{m_{pi}pi}\omega_{m_{pi}pi} \end{bmatrix}, \boldsymbol{E}_{pi} = \begin{bmatrix} \omega_{1pi}^2 & & & \\ & \omega_{2pi}^2 & & \\ & & \ddots & \\ & & & \omega_{m_{pi}pi}^2 \end{bmatrix}, \text{where } \rho_{jpi} \text{ is}$$

the attenuation coefficient of the j th flexibility mode of the i th flexible appendage, ω_{jpi} is the model frequency of the j th flexibility mode of the i th flexible appendage, m_{pi} is the number of flexible modes of the i th flexible appendage.

In this Chapter, the roll and yaw attitude of the satellite are controlled by using one MBMW that has gimballing capability. Therefore the total torque in the roll axis of the satellite, i.e. T_{sx} and the total torque in the yaw axis of the satellite, i.e. T_{sz} are composed of MBMW's electromagnetic torque, external environmental disturbance torque and internal disturbance torque caused by payload's mechanical movement. As usual, external environmental disturbance torque includes air drag torque, gravity gradient torque, solar radiation torque and magnetic torque.

6.2 SATELLITE ATTITUDE CONTROL SYSTEM

According to (6.1) and by ignoring the effect of flexible appendages, we know that the three axes of the satellite are independent. Therefore in the following sections we can only study the satellite attitude control in roll and yaw axes by using one MBMW.

As we know that the satellite's attitude motion varies much slower than the wheel's gimballing motion. Therefore, according to double control loops scheme proposed in [1], we can design satellite controller denoted as K_s and wheel controller denoted as K_w. Suppose that P_s and P_w represent the transfer functions of the plant to be controlled of the satellite and the MBMW, respectively. Then the satellite attitude control system by using MBMW is shown in Fig. 6.2. In Fig. 6.2, the transfer function from position command of MBMW to MBMW's electromagnetic torque, i.e. the block enclosed in dash-line frame is represented by H_w.

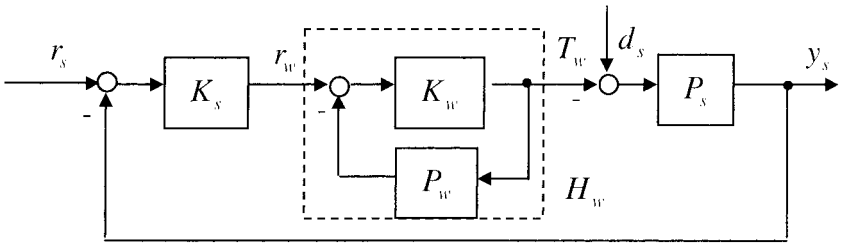

Fig. 6.2 Satellite attitude control system by using MBMW

6.2.1 Coordinate Transformation

In this report, the dynamic motion of MBMW is described in spin-free coordinate system $X_{2w}Y_{2w}Z_{2w}$, and the attitude motion of satellite is depicted in satellite body-fixed coordinate system $X_sY_sZ_s$. In the previous Chapters, ϕ_w, φ_w are measured with respect to the inertial coordinate system $X_0Y_0Z_0$, while in this chapter they should be measured against coordinate system $X_sY_sZ_s$.

The coordinate transformation from $X_0Y_0Z_0$ to $X_{2w}Y_{2w}Z_{2w}$ and the coordinate transformation from $X_sY_sZ_s$ to $X_0Y_0Z_0$ can be represented in the following matrixes.

1) Coordinate transformation from $X_0Y_0Z_0$ to $X_{2w}Y_{2w}Z_{2w}$

$$R_{0\to 2w}=\begin{bmatrix}\cos\varphi_w & \sin\varphi_w\cos\phi_w & \sin\varphi_w\sin\phi_w\\ -\sin\varphi_w & \cos\varphi_w\cos\phi_w & \cos\varphi_w\sin\phi_w\\ 0 & -\sin\phi_w & \cos\phi_w\end{bmatrix}. \tag{6.2}$$

2) Coordinate transformation from XsYsZs to $X_0Y_0Z_0$

$$R_{s\to 0}=\begin{bmatrix}\cos\varphi_s\cos\theta_s & -\sin\varphi_s & \cos\varphi_s\sin\theta_s\\ \cos\phi_s\sin\varphi_s\cos\theta_s+\sin\phi_s\sin\theta_s & \cos\phi_s\cos\varphi_s & \cos\phi_s\sin\varphi_s\sin\theta_s-\sin\phi_s\cos\theta_s\\ \sin\phi_s\sin\varphi_s\cos\theta_s-\cos\phi_s\sin\theta_s & \sin\phi_s\cos\varphi_s & \sin\phi_s\sin\varphi_s\sin\theta_s+\cos\phi_s\cos\theta_s\end{bmatrix}. \tag{6.3}$$

When ϕ_w, φ_w, ϕ_s, φ_s, θ_s are very small, (6.2) and (6.3) can be simplified as (6.4) and (6.5), respectively.

$$R_{0\to 2_w} \approx \begin{bmatrix} 1 & \varphi_w & 0 \\ -\varphi_w & 1 & \phi_w \\ 0 & -\phi_w & 1 \end{bmatrix}. \tag{6.4}$$

$$R_{s\to 0} \approx \begin{bmatrix} 1 & -\varphi_s & \theta_s \\ \varphi_s & 1 & -\phi_s \\ -\theta_s & \phi_s & 1 \end{bmatrix}. \tag{6.5}$$

Therefore so long as ϕ_w, φ_w, ϕ_s, φ_s, θ_s are very small, $X_sY_sZ_s$ measured ϕ_w and φ_w coincide to the first order with values measured in $X_0Y_0Z_0$.

6.2.2 MBMW Control Loop

As discussed in Chapter 3, define $J_{yw}/J_w = \sigma$, $\dot{\theta}_w = \Omega$, suppose the Euler angles of the satellite are small, then we can have the linearized dynamic model of MBMW, the linearized first-order model of electromagnets, and the model of gap sensors as follows.

$$\begin{cases} \ddot{\phi}_w - \sigma\Omega\dot{\varphi}_w = T'_x / J_w \\ \ddot{\varphi}_w + \sigma\Omega\dot{\phi}_w = T'_z / J_w \end{cases}. \tag{6.6}$$

$$\begin{cases} T'_x = k_{EM} v_\phi + k_N \phi_w \\ T'_z = k_{EM} v_\varphi + k_N \varphi_w \end{cases}. \tag{6.7}$$

$$\begin{cases} \tilde{\phi}_w = \phi_w + \xi_\phi \\ \tilde{\varphi}_w = \varphi_w + \xi_\varphi \end{cases}. \tag{6.8}$$

(6.6), (6.7) and (6.8) represent the plant to be controlled of MBMB, whose transfer function is P_w.

The MBMW is controlled by AMFC method. The AMFC control loop, i.e. K_w, is composed of the following parts.

3) Observer

$$\begin{cases} \phi_e = \left[\dfrac{a(k_{11}+k_{21})}{s^2(s+a)} + \dfrac{a(k_{12}+k_{22})}{s(s+a)}\right](\tilde{\phi}_w - \phi_e) + \dfrac{k_{EM0}}{J_{w0}s^2}u_x \\ \varphi_e = \left[\dfrac{a(k_{11}+k_{21})}{s^2(s+a)} + \dfrac{a(k_{12}+k_{22})}{s(s+a)}\right](\tilde{\varphi}_w - \varphi_e) + \dfrac{k_{EM0}}{J_{w0}s^2}u_z \end{cases} \tag{6.9}$$

4) Nutation Damping

$$\begin{cases} u_{nx} = -J_{wy0}\Omega_0 \dfrac{\kappa s^2}{s^2 + \kappa s + (\sigma_0\Omega_0)^2} \cdot \dfrac{b}{s+b}\tilde{\varphi}_w \\ u_{nz} = -J_{wy0}\Omega_0 \dfrac{\kappa s^2}{s^2 + \kappa s + (\sigma_0\Omega_0)^2} \cdot \dfrac{b}{s+b}\tilde{\phi}_w \end{cases}. \tag{6.10}$$

5) Non-linearity Compensator

$$\begin{cases} u_{cx} = -\dfrac{k_{N0}}{k_{EM0}}\phi_e \\ u_{cz} = -\dfrac{k_{N0}}{k_{EM0}}\varphi_e \end{cases}. \tag{6.11}$$

6) Gyro-decoupling Network

$$\begin{cases} u_{gx} = -\sigma_0\Omega_0\dfrac{1}{s}u_z \\ u_{gz} = \sigma_0\Omega_0\dfrac{1}{s}u_x \end{cases}. \tag{6.12}$$

7) PID Controller

$$\begin{cases} u_x = -(k_p + \dfrac{k_i}{s} + k_d s)(r_{w\phi} - \phi_e) \\ u_z = -(k_p + \dfrac{k_i}{s} + k_d s)(r_{w\varphi} - \varphi_e) \end{cases}. \tag{6.13}$$

Where $r_{w\phi}$ and $r_{w\varphi}$ are position commands of wheel in ϕ axis and φ axis, respectively.

8) Total Control

$$\begin{cases} v_\phi = \dfrac{1}{\tau s + 1}(u_x + u_{gx} + u_{cx} + u_{nx}) \\ v_\varphi = \dfrac{1}{\tau s + 1}(u_z + u_{gz} + u_{cz} + u_{nz}) \end{cases}, \tag{6.14}$$

where τ is time delay caused by electronic circuits and electromagnets.

Suppose $\zeta_\phi = 0$ and $\zeta_\varphi = 0$, denote $r_w = \begin{bmatrix} r_{w\phi} \\ r_{w\varphi} \end{bmatrix}$, then according to (6.6)～(6.14), we can derive the transfer functions from position command inputs to torque outputs of the MBMW, i. e. H_w, which is shown as follows.

$$\begin{cases} T_x = \dfrac{R_{21}G_{12} - R_{11}G_{22}}{G_{11}G_{22} - G_{12}G_{21}}r_{w\phi} + \dfrac{R_{22}G_{12} - R_{12}G_{22}}{G_{11}G_{22} - G_{12}G_{21}}r_{w\varphi} \\ T_z = \dfrac{R_{11}G_{21} - R_{21}G_{11}}{G_{11}G_{22} - G_{12}G_{21}}r_{w\phi} + \dfrac{R_{12}G_{21} - R_{22}G_{11}}{G_{11}G_{22} - G_{12}G_{21}}r_{w\varphi} \end{cases}. \tag{6.15}$$

Where

$$\begin{bmatrix} R_{11} & R_{12} \\ R_{21} & R_{22} \end{bmatrix} = \begin{bmatrix} k_{EM}E_{11}H_1 & k_{EM}E_{12}H_1 \\ k_{EM}E_{21}H_1 & k_{EM}E_{22}H_1 \end{bmatrix},$$

$$\begin{bmatrix} G_{11} & G_{12} \\ G_{21} & G_{22} \end{bmatrix} = \begin{bmatrix} \left[(k_{EM}F_{11}H_1+k_N)P_{11}+k_{EM}F_{12}H_1P_{21}\right]-1 & \left[(k_{EM}F_{11}H_1+k_N)P_{12}+k_{EM}F_{12}H_1P_{22}\right] \\ \left[(k_{EM}F_{22}H_1+k_N)P_{21}+k_{EM}F_{21}H_1P_{11}\right] & \left[(k_{EM}F_{22}H_1+k_N)P_{22}+k_{EM}F_{21}H_1P_{12}\right]-1 \end{bmatrix},$$

$$\begin{bmatrix} F_{11} & F_{12} \\ F_{21} & F_{22} \end{bmatrix} = \begin{bmatrix} -\left(F(PID)+\frac{k_{N0}}{k_{EM0}}\right)\frac{B}{A} & \sigma_0\Omega_0\frac{1}{s}\cdot\frac{B}{A}F(PID)-\frac{D}{C} \\ -\sigma_0\Omega_0\frac{1}{s}\cdot\frac{B}{A}F(PID)+\frac{D}{C} & -\left(F(PID)+\frac{k_{N0}}{k_{EM0}}\right)\frac{B}{A} \end{bmatrix},$$

$$\begin{bmatrix} E_{11} & E_{12} \\ E_{21} & E_{22} \end{bmatrix} = \begin{bmatrix} \frac{B-B_r}{A}F(PID)-\frac{k_{N0}}{k_{EM0}}\frac{B_r}{A} & -\sigma_0\Omega_0\frac{1}{s}\cdot\frac{B-B_r}{A}F(PID) \\ \sigma_0\Omega_0\frac{1}{s}\cdot\frac{A-B_r}{A}F(PID) & \frac{B-B_r}{A}F(PID)-\frac{k_{N0}}{k_{EM0}}\frac{B_r}{A} \end{bmatrix},$$

$$\begin{bmatrix} P_{11} & P_{12} \\ P_{21} & P_{22} \end{bmatrix} = \begin{bmatrix} \frac{1}{\left[s^2+(\sigma\Omega)^2\right]J_w} & \frac{\sigma\Omega}{\left[s^2+(\sigma\Omega)^2\right]J_w s} \\ \frac{-\sigma\Omega}{\left[s^2+(\sigma\Omega)^2\right]J_w s} & \frac{1}{\left[s^2+(\sigma\Omega)^2\right]J_w} \end{bmatrix},$$

$$\frac{B}{A} = \frac{a(k_{12}+k_{22})s+a(k_{11}+k_{21})}{s^3+as^2+a(k_{12}+k_{22})s+a(k_{11}+k_{21})+(s+a)F(PID)\frac{k_{EM0}}{J_{w0}}},$$

$$\frac{B_r}{A} = \frac{(s+a)F(PID)\frac{k_{EM0}}{J_{w0}}}{s^3+as^2+a(k_{12}+k_{22})s+a(k_{11}+k_{21})+(s+a)F(PID)\frac{k_{EM0}}{J_{w0}}},$$

$$\frac{D}{C} = J_{wy0}\Omega_0\frac{\varkappa s^2}{s^2+\varkappa s+(\sigma_0\Omega_0)^2}\cdot\frac{b}{s+b},$$

$$F(PID) = k_p+\frac{k_i}{s}+k_d s.$$

According to the frequency response of (6.15), we know that in low frequency domain ($0\sim 3\pi$), H_w can be approximated by (6.16).

$$H_w = \begin{bmatrix} J_w s^2 & -k_{wh}s \\ k_{wh}s & J_w s^2 \end{bmatrix}. \tag{6.16}$$

In (6.16), k_{wh} is a function of the rotational speed and the inertial moments of the MWMW. Let r represents wheel's rotational speed in rpm, then $k_{wh} \approx \gamma_{wh}(J_w,\sigma)\frac{r}{1000}$. Table 6.1 shows some examples of $\gamma_{wh}(J_w,\sigma)$ when $J_w = 0.0129$ kgm^2, $\sigma = 1.5$, $\sigma = 1.7$, $\sigma = 1.85$, and some parameters of the AMFC loop, i. e. k_{11}, k_{12}, k_{21}, k_{22} are selected as two-group typical values. According to Table 6.1 we know that k_{11}, k_{12}, k_{21}, k_{22} almost don't affect $\gamma_{wh}(J_w,\sigma)$.

Table 6.1 the relationship between $\gamma_{wh}(J_w, \sigma)$ and σ when $J_w = 0.0129$ kgm^2

$\gamma_{wh}(J_w,\sigma)$	$k_{11}=1,\ k_{12}=2$ $k_{21}=0,\ k_{22}=0$	$k_{11}=1,\ k_{12}=2$ $k_{21}=20,\ k_{22}=5$
$\sigma = 1.5$	1.9707	1.9708
$\sigma = 1.7$	2.2335	2.2335
$\sigma = 1.85$	2.5084	2.5084

6.2.3 Satellite Control Loop

Satellite attitude control loop consists of two parts. One part is a PID controller and the other part is the conversion from control command of satellite to wheel's position command.

If ignoring the effect of flexible appendages, the roll and yaw control of the satellite are independent and the plant to be controlled of the satellite can be expressed as follows.

$$\begin{cases} \phi_s = \dfrac{1}{J_{sx}s^2} T_{sx} \\ \varphi_s = \dfrac{1}{J_{sz}s^2} T_{sz} \end{cases}. \tag{6.17}$$

Design PID controller for (6.17), which can be expressed as follows.

$$\begin{cases} u_{sx} = -J_{sx}(k_{sp} + \dfrac{k_{si}}{s} + k_{sd}s)(r_{s\phi} - \phi_s) \\ u_{sz} = -J_{sz}(k_{sp} + \dfrac{k_{si}}{s} + k_{sd}s)(r_{s\varphi} - \varphi_s) \end{cases} \tag{6.18}$$

According to (6.16) and if $k_{wh} >> J_w$, then the conversion from satellite control commands to wheel position commands can be designed as follows.

$$\begin{cases} r_{w\phi} = -\dfrac{1}{k_{wh}} u_{sz} \\ r_{w\varphi} = \dfrac{1}{k_{wh}} u_{sx} \end{cases} \tag{6.19}$$

Therefore, the satellite controller K_s is composed of (6.18) and (6.19).

6.3 SIMULATION

Solar-A is selected for system simulation. The parameters of Solar-A are shown in Table 6.2 and Table 6.3. The parameters of MBMW are shown in Table 6.4. The parameters of wheel controller and satellite controller are shown in Table 6.5 and Table 6.6, respectively. Simulation conditions are shown in Table 6.7. The simulation results for system response to external environmental

disturbance, system response to internal disturbance due to fast movement of optical filters in on-board scientific instruments/optics-systems, and initial state response are shown in Fig. 6.3～Fig. 6.7, respectively. In these simulations, magnetic unloading of the MBMW which seems to be independent of the short-term performance is not considered. Hence, the rotor of the MBMW is touched down to the stator at 25[sec]. The magnetic unloading law will be considered in future work(s).

Table 6.2 inertial moments of Solar-A

Inertial moments (kgm^2)		
X axis	Y axis	Z axis
166.9	221.9	142.0

Table 6.3 flexibility characteristics of the solar paddles of Solar-A

Mode	frequency (Hz)	Conjunction coefficients						Attenuation Coefficient
		Paddle 1			Paddle 2			
		X	Y	Z	X	Y	Z	
1	1.99	-0.0283	-0.0016	-0.3678	+0.0238	-0.0016	+0.3678	≥0.002
2	2.19	+1.0866	+1.0846	+0.0285	-1.0866	+0.1846	-0.0285	≥0.002
3	7.55	+0.5703	+0.1644	+0.0630	-0.5703	+0.1644	-0.0630	≥0.002
4	7.81	+0.0494	+0.0483	+0.5445	-0.0494	+0.0483	-0.5445	≥0.002

Table 6.4 parameters of MBMW

J_w	σ	k_{EM}	$k_{N\phi}$ ($k_{N\varphi}$)	V_b	N_s	ϕ_g	φ_g	c_1,c_3,c_5	c_2,c_4,c_6
0.0129 kgm^2	1.85	0.0448 Nm/V	3.4225 Nm	0.8 V	6	0.6 deg	0.6 deg	0.004 deg	0.0005 deg

Table 6.5 parameters of MBMW control loop

$\varkappa$	b	$k_p gain$	$k_i gain$	$k_d gain$	k_{11}	k_{12}	k_{21}	k_{22}	a	k_{nut}	k_{logic}	δ_1	δ_2
32	10	121.2	150	15.64	1	2	0/20	0/5	25	k_{EM0}	5	10^{-5}	0.0035

Table 6.6 parameters of satellite control loop

k_{sp}	k_{si}	k_{sd}	k_{wh}
121.2	150	15.64	1.9707

Table 6.7 Simulation conditions

External disturbance	Internal disturbance	Initial state
0.001 Nm step disturbance in X axis	0.87 Nm in Z axis, interval 10 msec	$\phi_{s0} = 0.001\text{deg}, \varphi_{s0} = 0.0\text{deg}$

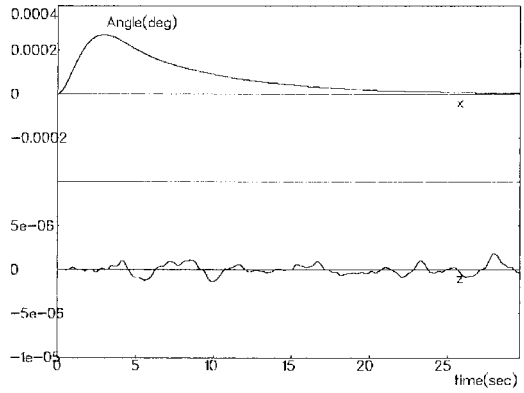

(a) attitude angles of satellite

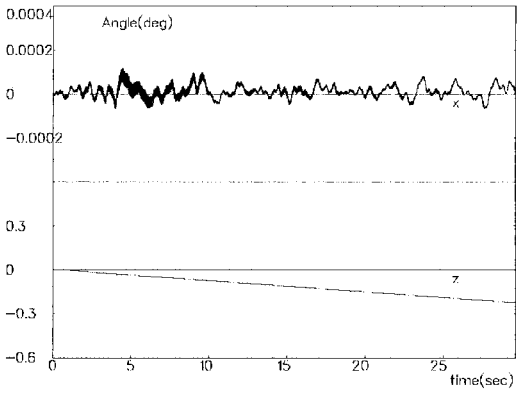

(b) gimballing angles of MBMW

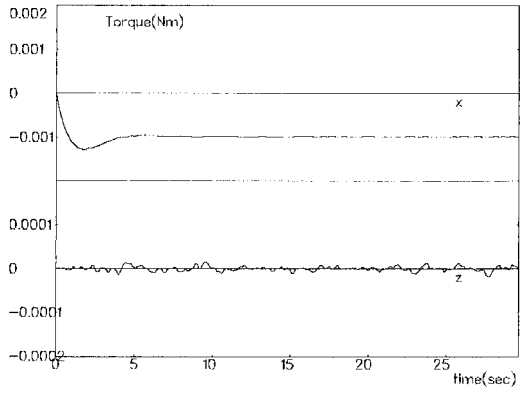

(c) control command of satellite

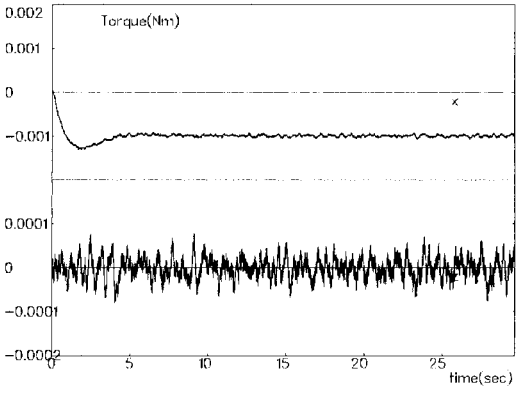

(d) MBMW's electromagnetic torque

Fig. 6.3 Response to external disturbance, $r = 3000rpm$

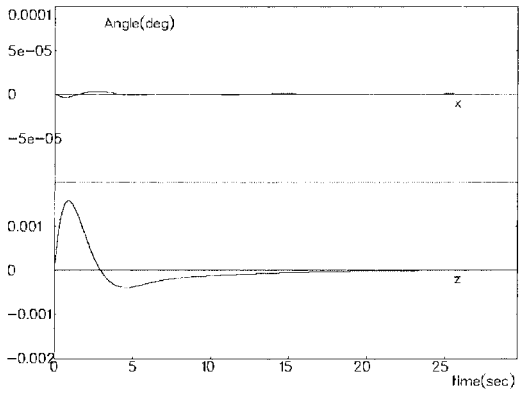

(a) attitude angles of satellite

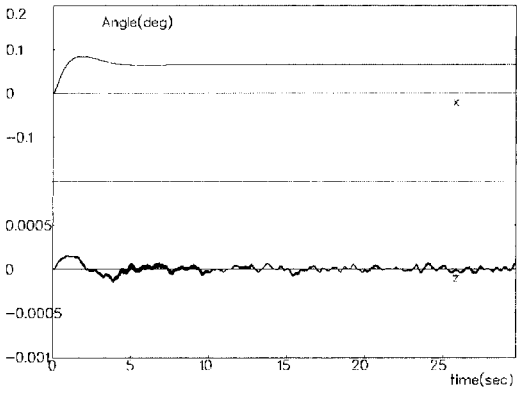

(b) gimballing angles of MBMW

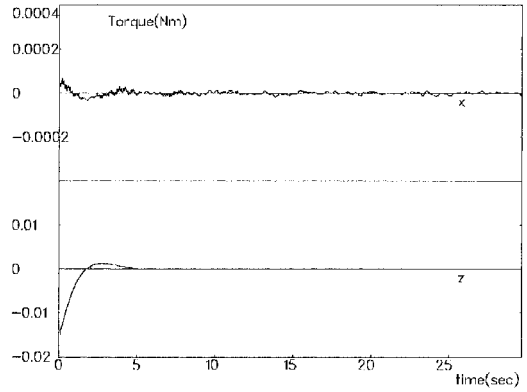

(c) control command of satellite

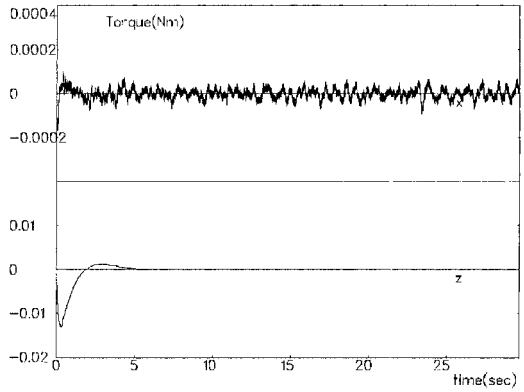

(d) MBMW's electromagnetic torque

Fig. 6.4 Response to internal disturbance, $r = 3000rpm$

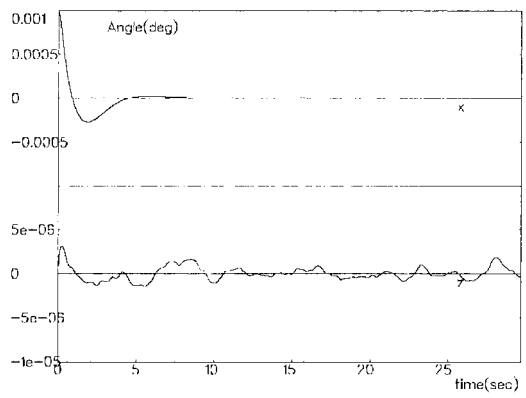

(a) attitude angles of satellite

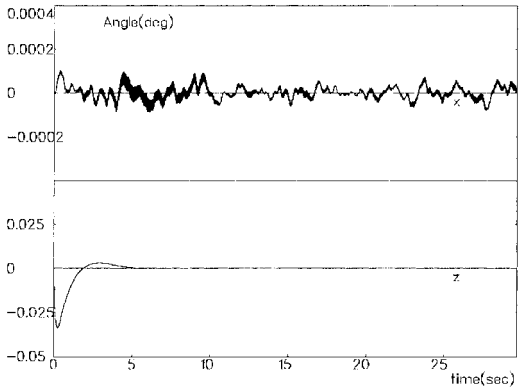

(b) gimballing angles of MBMW

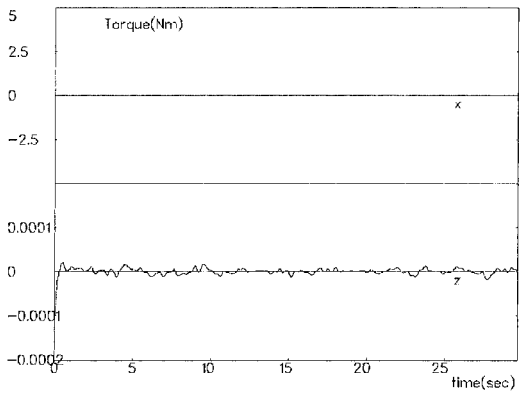

(c) control command of satellite

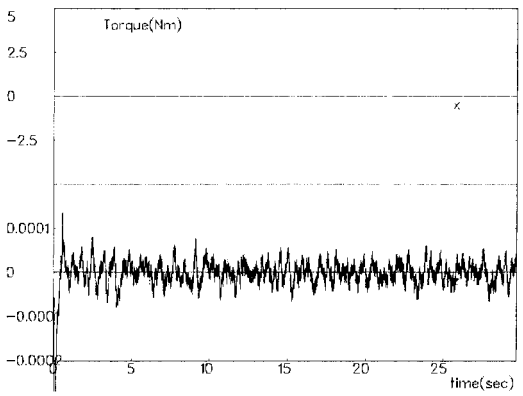

(d) MBMW's electromagnetic torque

Fig. 6.5 Initial state response, $r = 3000rpm$

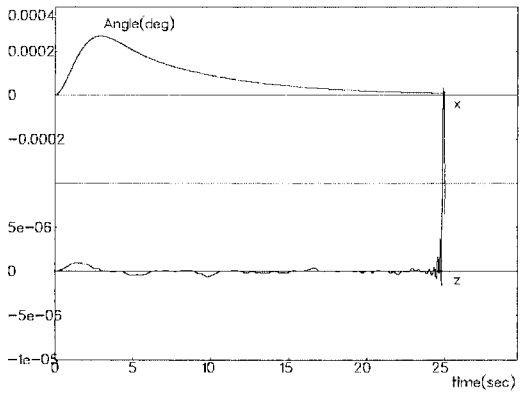

(a) attitude angles of satellite

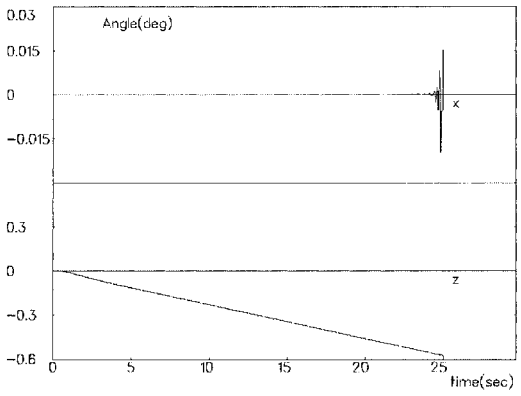

(b) gimballing angles of MBMW

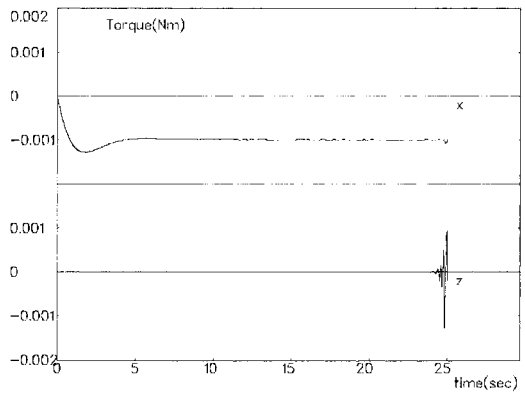

(c) control command of satellite

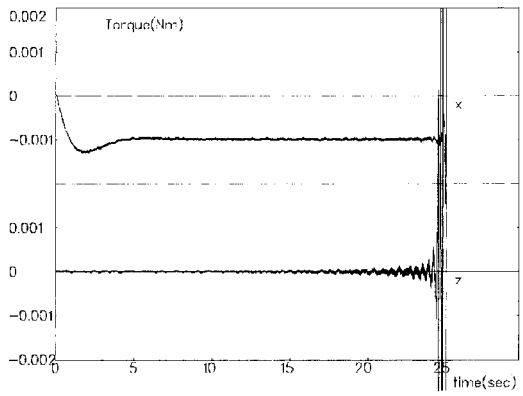

(d) MBMW's electromagnetic torque

Fig 6.6 Response to external disturbance, $r = 1000rpm$

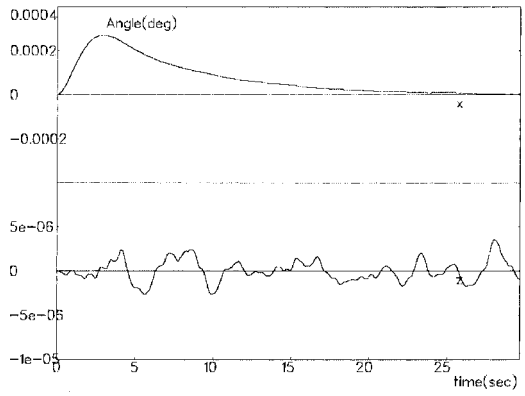

(a) attitude angles of satellite

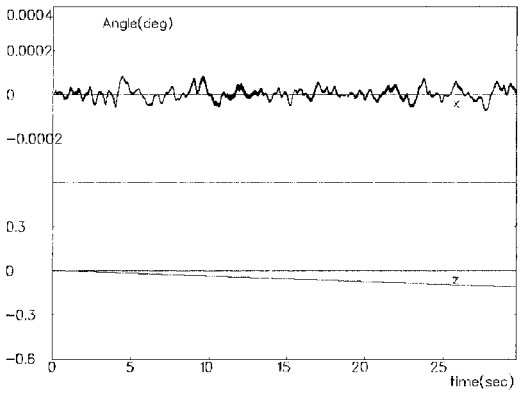

(b) gimballing angles of MBMW

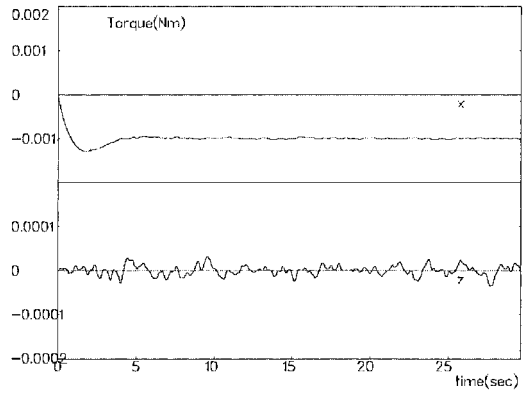

(c) control command of satellite

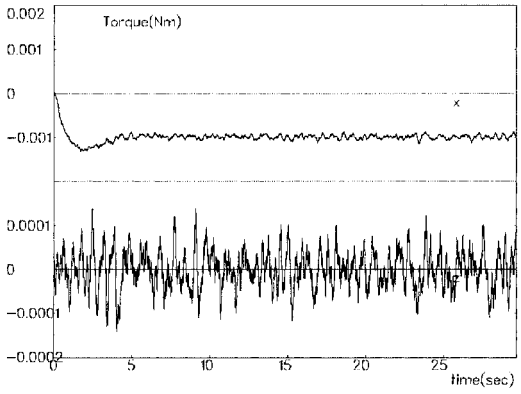

(d) MBMW's electromagnetic torque

Fig 6.7 Response to external disturbance, $r = 6000rpm$

Simulation results show that the MBMW controlled by AMFC method can make the satellite control system stable and obtain high accuracy attitude control for a large range of wheel rotational speed if angular momentum unloading is added in time to prevent wheel's touching down. Simulation results also show that high wheel rotational speed let the wheel have strong gimballing control capability.

In this Chapter the MBMW controlled by AMFC method is applied to the attitude control of satellite with flexible appendages. The low noise feature of MBMW controlled by AMFC method is demonstrated.

7 CONCLUSION

For the high-accuracy attitude control of spacecraft, MBMW has been being investigated as an actuator because of its merits of low disturbance characteristics and gimballability. The main problem in applying MBMW to spacecraft attitude control is the active control of MBMW. The active control of MBMW in this report means to make the rotor spin around its principal axis of inertia to achieve low disturbance purpose while being able to tilt the principal axis of inertia for attitude control of spacecraft, and this has to be done with adequate nutation damping.

In this report adaptive model following control method is presented for the active control of MBMW. This method relies on adaptive bandwidth-regulation mechanism, controller with logical derivative, new nutation damping network and non-linearity compensator. Consequently this method is convenient to make compromise between dynamic response and active-vibration suppression at harmonic frequencies of the wheel rotation, and to damp nutation of the wheel rotor while keeping the closed-loop system stable.

Study results show that this method has great capability of active-vibration suppression, good dynamic response, and satisfactory nutation damping for a large range of wheel rotational speed. The robustness of this method with respect to system uncertain parameters is also strong. Therefore it is easy and possible to realize high-accuracy spacecraft attitude control by using the MBMW controlled by the AMFC method. Now, applying the MBMW controlled by the AMFC method to spacecraft attitude control is under going.

ACKNOWLEDGEMENTS

The research concluded in this report was done during the first author's stay at Institute of space and Astronautical Science (ISAS) as C.O.E. research fellow on leaving from Beijing Institute of Control Engineering. The author firstly wants to express her honest thanks to Prof. Nishida, the Director General of ISAS for giving her a chance to work in ISAS. The author is grateful to her Chinese supervisor Prof. Yang Jiachi for his kind help to let the author come to ISAS and his constant encouragement.

The authors appreciate Dr. Inoue, Mr. Yoshida and Mr. Horiuchi of Mitsubishi Electric Corporation for their useful comments and discussions.

REFERENCES

[1] M. -R. Nam, T. Hashimoto and K. Ninomiya: Design of H_∞ Attitude Controllers for Spacecraft Using a Magnetically Suspended Momentum Wheel. European Journal of Control (1997), No.3, 114-124.

[2] U. J. Bichler: A Low Noise Magnetic Bearing Wheel for Space Application. 2 nd International Symposium on Magnetic Bearing, July 12-14, 1990, Tokyo, Japan, 1-8.

[3] Yong-Chun Xie, Hong-Xin Wu and Zhen-Duo Lu: The All-Coefficient Adaptive Control Method and Its Application in Spacecraft Attitude Control. Space Technology, Vol.16, No.5/6, pp.331-336, 1996.

[4] R. Herzog, P. Buhler, C. Gahler, and R. Larsonneur: Unbalance Compensation Using Generalized Notch Filters in the Multivariable Feedback of Magnetic Bearings, IEEE Transactions on Control Systems Technology, Vol. 4, No.5, Sep. 1996, 580-586.

[5] M. Ahrens, L. Kučera, and R. Larsonneur: Performance of a Magnetically Suspended Flywheel Energy Storage Device, IEEE Transactions on Control Systems Technology, Vol. 4, No.5, Sep. 1996, 494-502.

[6] F. Matsumura, T. Namerikawa K. Hagiwara, and M. Fujita, Application of Gain ScheduledH_∞ Robust Controllers to a Magnetic Bearing, IEEE Transactions on Control Systems Technology, Vol. 4, No.5, Sep. 1996, 484-493.

[7] K. Nonami and T. Ito, μ Synthesis of Flexible Rotor-Magnetic Bearing Systems, IEEE Transactions on Control Systems Technology, Vol. 4, No.5, Sep. 1996, 503-512.

[8] A. E. Rundell, S. V. Drakunov, and R. A. DeCarlo, A Sliding Mode Observer and Controller for Stabilization of Rotational Motion of a Vertical Shaft Magnetic Bearing, IEEE Transactions on Control Systems Technology, Vol. 4, No.5, Sep. 1996, 598-608.

[9] C. R. Burrows and M. N. Sahinkaya, Vibration Control of Multimode Rotor-bearing Systems, Proc. Roy. Soc. Lond. A, vol. 386, 1983, 77-94.

[10] M. Fujita, F. Matsumura, and M. Shimizu, H_∞ Robust Control Design for a Magnetic Suspension System, 2 nd International Symposium on Magnetic Bearing, July 12-14, 1990, Tokyo, Japan, 349-356.

[11] A. Charara, J. De Miras, and B. Caron, Nonlinear Control of Magnetic Levitation System Without Premagnetization, IEEE Transactions on Control Systems Technology, Vol. 4, No.5, Sep. 1996, 513-523.

[12] F. Mastumura, M. Fujita, and K. Okawa, Modeling and Control of Magnetic Bearing Systems Achieving a Rotation Around the Axis of Inertia, 2 nd International Symposium on Magnetic Bearing, July 12-14, 1990, Tokyo, Japan, 273-280.

[13] T. Higuchi and m. Otsuka, Identification of Rotor Unbalance and Reduction of Housing Vibration by Periodic Learning Control in Magnetic Bearings, 3 rd International Symposium on Magnetic Bearing, July 1992, Alexandria, VA, 571-579.

[14] C. R. Knospe, Robustness of Unbalance Response Controllers, 3 rd International Symposium on Magnetic Bearing, July 1992, Alexandria, VA, 580-589.

[15] S. Beale, B. Shafal, P. Larocca, and E. Cusson, Adaptive Forced Balancing for Magnetic Bearing Systems, 3 rd International Symposium on Magnetic Bearing, July 1992, Alexandria, VA, 601-611.

[16] C. R. Knospe, R. W. Hope, S. J. Fedigan, and R. D. williams, New Results in the Control of Rotor Synchronous Vibration, 4 th International Symposium on Magnetic Bearing, August, 1994, ETH Zurich, 119-124.

[17] T. Higuchi, T. Mizuno, and M. Tsukamoto, Digital Control System for Magnetic Bearings with Automatic Balancing, 2 nd International Symposium on Magnetic Bearing, July 12-14, 1990, Tokyo, Japan, 27-32.

[18] K. Nonami and H. Yamaguchi, Robust Control of Magnetic Bearing Systems by Means of Sliding Mode Control, 3 rd International Symposium on Magnetic Bearing, July 1992, Alexandria, VA, 537-546.

[19] K. -Y. Lum, V. T. Coppola, and D. S. Bernstein, Adaptive Autocentering Control for an Active Magnetic Bearing Supporting a Rotor with Unknown Mass Imbalance, IEEE Transactions on Control Systems Technology, Vol. 4, No.5, Sep. 1996, 587-597.

[20] H. Koskinen, O. Lindgren, and O. Karasti, Fuzzy Logic in Active Magnetic Bearing Control, 4 th International Symposium on Magnetic Bearing, August, 1994, ETH, Zurich, 89-93.

[21] N. K. Rutland, P. S. Keogh and C. R. Burrows, Comparison of Controller Designs for Attenuation of Vibration in

a Rotor-bearing System Under Synchronous and Transient Conditions, 4 th International Symposium on Magnetic Bearing, August, 1994, ETH Zurich, 107-112.

[22] Y. Kanemitsu M. Ohsawa, and E. Marui, Comparison of Control Laws for Magnetic Levitation, 4 th International Symposium on Magnetic Bearing, August, 1994, ETH, Zurich, 13-18.

[23] U. Bichler, T. Eckardt, A 3(5) Degree of Freedom Electro-dynamic Bearing Wheel for 3-axis Spacecraft Attitude Control Applications, proceedings of the First International Symposium on Magnetic Bearings, June 6-8, 1998, ETH Zurich, 13-22.

[24] C. Murakami, Digital Control of Conical Motion of High Speed Rotors Suspended by Magnetic Bearings in Case of Large Sampling Period, 4 th International Symposium on Magnetic Bearing, August, 1994, ETH, Zurich, 7-12.

[25] U. Bichler, T. Eckardt, A 3(5) Degree of Freedom Electro-dynamic Bearing Wheel for 3-axis Spacecraft Attitude Control Applications, proceedings of the First International Symposium on Magnetic Bearings, June 6-8, 1988, ETH Zurich,1-8.

[26] Inoue M, Ninomiya K., Stability and Control of Attitude Motion of a Satellite Equipped with a Magnetic Wheel, Journal of SICE, vol. 25, No.10, 1989 (in Japanese), 1104-1105.

[27] Hashimoto T, Hamasaki T, Nakatani I, Ninomiya K. Attitude Control System Design of a Satellite with a Magnetically Suspended Momentum Wheel Based on Two-Degree-of-Freedom Control System Theory. AIAA Guidance, Navigation, and Control conference, Monterey, CA, Aug. 9-11, 1993, 1285-1294, AIAA-93-3844-CP.

[28] Myeong-Ryong Nam, Studies on the Attitude Control System for Spacecraft Employing a Magnetically-Suspended Momentum Wheel, Doctoral Dissertation, University of Tokyo, 1997.

[29] Yasushi Horiuchi and Masao Inoue, Parameters for MBMW Simulation, Mitsubish Electric Corporation, 1999, (private communication).

REPORTS ALREADY PUBLISHED

No.665(March 1996)
Drago MATKO, Nobuyuki YAJIMA and Motoki HINADA : Adaptive Balloon Azimuth Control using a Simple DC Motor Actuator

No.666(February 1997)
Kyoichi KURIKI, Mitsuru TAKEI, Noboru WAKASUGI and Tetsuo YASAKA : Meteoroid and Space Debris Impact Investigations in SFU post Flight Analysis Activities : Preliminary Results and Further Directions

No.667(March 1997)
Ho Sang KWAK and Kunio KUWAHARA : Transient Cooling of an Enclosed Fluid through Its Maximum-Density Temperature

No.668(March 1997)
Ho Sang KWAK and Kunio KUWAHARA : Thermal Convection of an Enclosed Fluid Responding to Time-Periodic External Excitations : Effects of g-jitters and wall temperature oscillation

No.669(September 1997)
Kazuhisa FUJITA and Takashi ABE : SPRADIAN, Structured Package for Radiation Analysis : Theory and Application

No.670(September 1997)
Shin-ichi TSUDA, Hirotaka AOKI and Takuya OKUMOTO : Nonholonomic Space Robot Path Planning for Spacecraft Attitude Stabilization and Control

No.671(March 1998)
Chiyoe KOIKE and Hiroshi SHIBAI : The Infrared Spectra of Candidate Materials for Celestial Dust by Laboratory Measurements

No.672(March 1999)
Takahiro KAWASHIMA, Kohichiro OYAMA and Katsuhisa SUZUKI : A Measurement of Vibrational-Rotational Temperature and Density of Molecular Nitrogen in the Upper Atmosphere by Rocket-Borne Electron Beam Induced Luminescence

No.673(March 1999)
Tsutomu T. TAKEUCHI, Hiroyuki HIRASHITA, Kouji OHTA, Takako T. ISHII and Kohji YOSHKAWA : Simulation of the IRIS Far-infared Survey : A Guide for Infrared Galaxy Number Counts

No.674(March 1999)
Kuniko KUWAHARA and Karl G. ROESNER : Shock Wave Development around Accelerated Bodies at Supersonie Mach Numbers Slightly Larger than One

No.675(September 1999)
K. K. MAHAJAN and Kohichiro OYAMA : Venus Ionosphere : Major Features

No.676(March 2000)
Kojiro SUZUKI, Hiroaki HIMEKI, Tadaharu WATANUKI and Takashi ABE : Experimental Studies on Characteristics of Shock Wave Propagation through Cylinder Array

No.677(March 2000)
Hiroaki SHIRAISHI, Satoshi TANAKA, Masahiko HAYAKAWA, Akio FUJIMURA and Hitoshi MIZUTANI : Dynamical Characteristics of Planetary Penetrator : Effect of Incidence Angle and Attack Angle at Impact

No.678(July 2000)
K. NOGUCHI, T. IMAMURA and K.-I.OYAMA : A Feasibility Study for Observing Small Lunar and Martian Ionospheres by Radio Occultation Technique

No.679(March 2001)
Takashi WATANABE, Katsuhisa SUZUKI and Kohichiro OYAMA : Observation of Stratospheric Ozone with MT-135 Rockets in 1990-1999